JACS
JOURNAL OF THE AMERICAN CHEMICAL SOCIETY
Article
Cite This: J. Am. Chem. Soc. 2017, 139, 16803-16812
pubs.acs.org/JACS

Well-Defined Silanols in the Structure of the Calcined High-Silica Zeolite SSZ-70: New Understanding of a Successful Catalytic Material

Stef Smeets,[*,†,∥] Zachariah J. Berkson,[‡] Dan Xie,[§] Stacey I. Zones,[§] Wei Wan,[∥] Xiaodong Zou,[∥] Ming-Feng Hsieh,[‡,⊗] Bradley F. Chmelka,[‡] Lynne B. McCusker,[†,‡] and Christian Baerlocher[†,‡]

[†]Laboratory of Crystallography, ETH Zurich, Vladimir-Prelog-Weg 5, Zurich CH 8093, Switzerland
[‡]Department of Chemical Engineering, University of California, Santa Barbara, California 93106, United States
[§]Chevron Energy Technology Company, Richmond, California 94802, United States
[∥]Berzelii Center EXSELENT on Porous Materials, Department of Material and Environmental Chemistry, Stockholm University, SE-106 91 Stockholm, Sweden

Supporting Information

ABSTRACT: The structure of the calcined form of the high-silica zeolite SSZ-70 has been elucidated by combining synchrotron X-ray powder diffraction (XRPD), high-resolution transmission electron microscopy (HRTEM), and two-dimensional (2D) dynamic nuclear polarization (DNP)-enhanced NMR techniques. The framework structure of SSZ-70 is a polytype of **MWW** and can be viewed as a disordered ABC-type stacking of **MWW**-layers. HRTEM and XRPD simulations show that the stacking sequence is almost random, with each layer being shifted by ±1/3 along the ⟨110⟩ direction with respect to the previous one. However, a small preponderance of ABAB stacking could be discerned. DNP-enhanced 2D ^{29}Si{^{29}Si} *J*-mediated NMR analyses of calcined Si-SSZ-70 at natural ^{29}Si isotopic abundance (4.7%) establish the through-covalent-bond ^{29}Si−O-^{29}Si connectivities of distinct Si sites in the framework. The DNP-NMR results corroborate the presence of **MWW** layers and, more importantly, identify two distinct types of Q^3 silanol species at the surfaces of the interlayer regions. In the first, an isolated silanol group protrudes into the interlayer space pointing toward the pocket in the adjacent layer. In the second, the surrounding topology is the same, but the isolated −SiOH group is missing, leaving a nest of three Si−O−H groups in place of the three Si−O−Si linkages. The analyses clarify the structure of this complicated material, including features that do not exhibit long-range order. With these insights, the novel catalytic behavior of SSZ-70 can be better understood and opportunities for enhancement recognized.

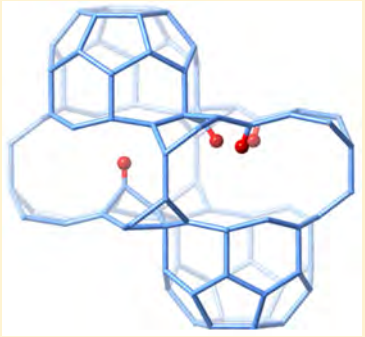

INTRODUCTION

Zeolite molecular sieves have nanoporous architectures with pore openings that are typically less than 1 nm in diameter. The tetrahedrally coordinated Si atoms in the silicate framework structure may also be replaced with other elements such as Al, and this can lead to charge imbalance and an opportunity for additional cations to be introduced into the structure. If protons are used to counterbalance such Al^{3+} sites, very strong acid catalysts can be created, and these have a great impact in a large variety of chemical and petrochemical processes.[1] In particular, they are used to promote catalytic rearrangement reactions in which the location of the acid sites within the zeolite structure have a strong effect on the selectivity and activity for a given reaction.[2] The nanopore architecture and composition of a zeolite are important factors in controlling the transition states between reactants and products within the confining nanopores.[3] Furthermore, the diffusion pathways for the products, which are influenced by the details of the zeolite structure (and crystallite size), also play a significant role in the selectivity.[4]

Indeed, there is an increasing understanding that instead of focusing on the entire zeolite structure, portions of the internal zeolite architecture can be exploited in an optimal fashion to design the catalytic sites. Excellent recent examples include (1) the development of a novel carbonylation catalyst using only a subdomain of the zeolite mordenite,[5,6] (2) the creation of acid sites in only the large pores of a borosilicate zeolite where there are both large and small pores and boron has been selectively replaced postsynthetically with aluminum,[2,7] and (3) an elegant effort to synthesize a zeolite using an organic structure directing agent (OSDA) designed to mimic the structure of the desired transition state of a reaction.[8] These advances broaden our view of how to use zeolites as catalysts, going beyond the previous boundaries of just focusing on the size of the pores. Consequently, understanding the fine and local structural details of a new zeolite is essential for designing an optimal catalyst.

Here, we present a comprehensive structural analysis of the novel zeolite SSZ-70, which has already begun to emerge as an important and novel catalytic material. SSZ-70 was first synthesized in borosilicate form when Zones and Hwang

Received: August 31, 2017
Published: October 25, 2017

DOI: 10.1021/jacs.7b08810
J. Am. Chem. Soc. 2017, 139, 16803−16812

were exploring a system featuring both borosilicate inorganic reaction conditions and HF as a mineralizer (in contrast to the conventional alkaline type of reaction normally used in zeolite syntheses).[9] In this environment and using *N*,*N*′-diisopropylimidazolium, which has very high selectivity for **MTT**-type frameworks under alkaline conditions,[10] as the OSDA, the novel phase B-SSZ-70 was formed.[11]

In a later study, Archer and co-workers[12] extended the range of imidazolium-type OSDAs that favor the formation of SSZ-70. They also showed that aluminosilicate analogues (Al-SSZ-70) could be made and developed the synthesis chemistry to allow alkaline media to be used instead of HF. Scanning electron microscopy (SEM) images of these materials showed them to be platelets, as would be expected for a layered material, and their X-ray powder diffraction (XRPD) patterns contained both broad and sharp peaks, which would be consistent with well-ordered layers stacked in a somewhat disordered fashion. Further characterization by magic angle spinning (MAS) nuclear magnetic resonance (NMR) showed that SSZ-70 was related to, but distinctly different from, MCM-22[13] (**MWW**-type framework structure),[14] which has already been developed as a commercial catalyst for the alkylation of aromatics.[15] MCM-22 and its **MWW**-type analogues (e.g., ITQ-1[16] and SSZ-25[17]) are unique among the known zeolites in that they only form the fully 4-connected **MWW**-type framework upon calcination. The as-synthesized materials are layered (alumino)silicates that lend themselves to exfoliation.

In view of these observations, it appeared that as-synthesized SSZ-70 was likely to be organized in layers, so exfoliation procedures were applied, and indeed, exfoliated Al-SSZ-70 was found to exhibit enhanced catalysis rates for alkylation reactions.[18] In the calcined form, Al-SSZ-70 exhibits high activity as a cracking catalyst, and subsequent deactivation is different from that of SSZ-25 (**MWW**), which becomes more selective with coking.[19] This difference in catalytic performance indicates that there are some key differences in the structural details of zeolites SSZ-25 and 70, even though both are built from similar layers. With more structural information, we hoped to rationalize the different activities of SSZ-70 as a catalyst when the material has been delaminated and certain external features at the surface of the crystalline zeolite modified. The replacement of boron sites located in wells along the interlayer surface of B-SSZ-70 with other heteroatoms, for example, has proven to be particularly effective in creating catalysts that are suitable for larger reactant molecules, while retaining the important confinement features of a zeolite catalyst.[18,20] We also wanted to understand why the structure of SSZ-70 lends itself to delamination via more gentle, nondestructive conditions, which allow the integrity of the boron replacement sites in the surface structure to be retained.[21] Most of the previous delamination work on other zeolite materials required harsh basic conditions that led to some amorphization of the materials, which is detrimental to the catalytic properties.[22]

We realized early on that a straightforward determination of the structure of SSZ-70 from diffraction data would not be possible, because of the disorder in the material. Therefore, we combined three highly complementary state-of-the-art techniques to elucidate the structure. Here, we present the structure of calcined siliceous SSZ-70, as determined from a combination of high-resolution transmission electron microscopy (HRTEM), synchrotron X-ray powder diffraction (XRPD), and dynamic-nuclear-polarization (DNP)-enhanced MAS NMR spectroscopy data.

EXPERIMENTAL SECTION

Synthesis of Si-SSZ-70. Tetraethyl orthosilicate (6 mmol, 1.26 g) and 3 mmol of *N*,*N*′-diisobutylimidazolium hydroxide (Figure 1, 6.66 g of solution) were added to a tared cup and cap (Teflon) of a small Parr reactor. The top was tightly closed, and the reactants were allowed to hydrolyze the silicate for 3 days. Afterward, the top was lifted, and the internal reactor contents were exposed to an air draft in a hood to remove ethanol and water slowly. When the reactor contents had been reduced to near dryness (requiring several days) the reactor and top were weighed again. The H_2O/SiO_2 molar ratio was then adjusted to 7 by adding water in small amounts to the reaction mixture. After stirring, 50% HF was added by mass to add 3 mmol (about 0.12 g) of reagent. The reactor was closed and heated to 150 °C while being tumbled at 43 rpm for 8 days. The reactor was then removed from the oven and allowed to cool to room temperature.

The Al-SSZ-70 material was synthesized according to the protocol described in ref 12 using *N*,*N*′-diisobutylimidazolium hydroxide as the OSDA.

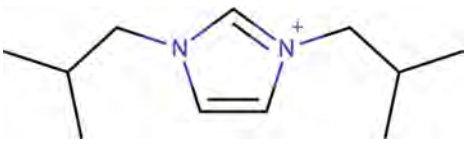

Figure 1. *N*,*N*′-Diisobutylimidazolium cation that was used as the organic structure-directing agent in the syntheses of SSZ-70.

Calcination. To simplify the complicated structure analysis, the material was calcined to remove the OSDA. A thin bed of the zeolite sample was calcined in air in a muffle furnace with a controlled ramp program: temperature increased at a rate of 1 °C per minute up to 120 °C; held for 2 h; increased at the same rate up to 540 °C; held for 5 h; and finally allowed to cool down slowly in the oven.

X-ray Powder Diffraction. Synchrotron XRPD data were collected on both calcined and as-synthesized samples of Si-SSZ-70 and Al-SSZ-70 in a rotating 0.3 mm capillary on the MS-Powder beamline at the Swiss Light Source in Villigen, Switzerland (wavelength 0.70848 Å, MYTHEN II detector).[23]

Electron Microscopy. Scanning electron micrographs (Figure 2) were obtained using a JEOL JSM 6700F instrument. For high-resolution transmission electron microscopy (HRTEM) analysis, a sample of as-synthesized Al-SSZ-70 was mixed with ethanol, treated by ultrasonication, then transferred to a copper grid covered with lacey carbon and dried in air. Using a 200 kV JEOL JEM-2100F

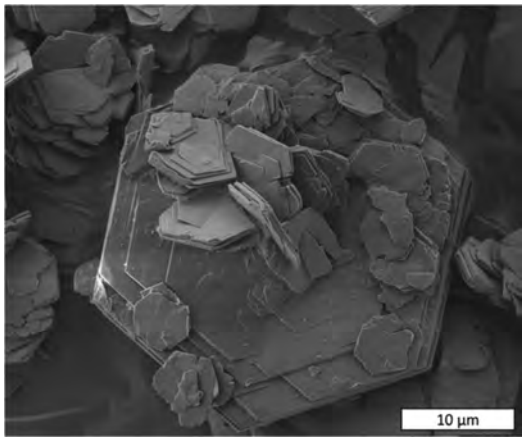

Figure 2. SEM image of as-synthesized Al-SSZ-70.

DOI: 10.1021/jacs.7b08810
J. Am. Chem. Soc. 2017, 139, 16803−16812

transmission electron microscope equipped with a Gatan UltraScan 1000 camera, 20 HRTEM images were taken under the same conditions (close to the Scherzer focus) with a weak electron beam. These were then summed together into a single image, after correcting for sample drift by cross correlation, to improve the signal-to-noise ratio, following the approach described by Xie and co-workers.[24]

Solid-State NMR Spectroscopy. DNP-enhanced MAS NMR techniques at low temperatures (ca. 100 K)[25−32] provide significantly enhanced NMR signal sensitivity that allows the detection and analysis of ^{29}Si environments in zeolite frameworks at natural isotopic abundance (4.7%).[33−38] More explanatory details of the DNP-NMR methods and analyses are provided in the Supporting Information.

All solid-state DNP-enhanced ^{29}Si{^{29}Si} and ^{29}Si{^{1}H} NMR experiments were carried out on a Bruker ASCEND 400 DNP-NMR spectrometer with a 9.4 T superconducting magnet operating at 399.95 and 79.46 MHz for ^{1}H and ^{29}Si nuclei, respectively, and equipped with a gyrotron and microwave transmission line capable of providing 263 GHz microwave irradiation at the sample and a low-temperature 3.2 mm triple-resonance MAS probehead. The DNP-enhanced ^{29}Si{^{1}H} and ^{29}Si{^{29}Si} spectra were acquired at 95 K, 8 kHz MAS, under continuous microwave irradiation at 263 GHz, and in the presence of 16 mM TEKPol biradical[39] in frozen 1,1,2,2-tetrachloroethane (TCE). Before NMR analyses, the calcined Si-SSZ-70 material was dried overnight at 200 °C to remove adsorbed water. The sample was prepared in a dry glovebox and was mixed under incipient wetness conditions.[40,36] The ^{29}Si DNP-NMR signal enhancement was quantified as the ratio of the fully relaxed ^{29}Si{^{1}H} CPMAS signal intensities obtained with and without continuous microwave irradiation and was measured to be ca. 16.

The DNP-enhanced solid-state 2D *J*-mediated ^{29}Si{^{29}Si} spectrum[38,41,42] was acquired using ^{29}Si{^{1}H} cross-polarization with a 2.5 μs ^{1}H excitation pulse and a contact time of 4 ms to circumvent the effects of the long ^{29}Si spin−lattice relaxation times. The efficiency of the 2D ^{29}Si{^{29}Si} *J*-mediated experiment depends on the ratio of ^{29}Si relaxation parameters T_2'/T_2*, which was measured to be 11 or greater for all of the ^{29}Si signals (Supporting Information). The spectrum was acquired with an experimentally optimized half-spin−echo (τ) delay of 8 ms, ^{29}Si $\pi/2$ and π pulse lengths of 5 and 10 μs, respectively, a repetition time of 3 s, 32 t_1 increments, a rotor-synchronized incremental step size of 125 μs, and 2048 transients for a total acquisition time of 54 h. Additional experimental details are provided in the Supporting Information.

The DNP-enhanced 2D ^{29}Si{^{1}H} HETeronuclear CORrelation (HETCOR) spectra were acquired using 0.2 or 5 ms contact times, 80 or 160 t_1 increments, an incremental step size of 64 μs, 64 or 16 transients, and repetition times of 3 s for total acquisition times of 4 or 2 h. The ^{29}Si{^{1}H} DNP-HETCOR spectra were acquired using eDUMBO-1$_{22}$ homonuclear coupling during the ^{1}H evolution period to improve resolution in the ^{1}H dimension.[43] All ^{29}Si NMR spectra were acquired using 100 kHz SPINAL-64 ^{1}H decoupling during the acquisition period.[44]

RESULTS AND DISCUSSION

Long-Range Order in Si-SSZ-70. Synchrotron X-ray powder diffraction (XRPD) data were collected on as-synthesized and calcined samples of Al- and Si-SSZ-70 (Figure 3). We started our analysis with the XRPD data for as-synthesized Si-SSZ-70. Although the pattern contains a mixture of broad and sharp reflections, it could still be indexed with a hexagonal unit cell ($P6_3/mmc$, a = 14.223 Å, c = 53.786 Å). SSZ-70 crystallizes in the form of well-defined hexagonal flakes approximately 50 nm in thickness (Figure 2), and this is consistent with the unit cell and space group symmetry. The a lattice parameter is similar to and the c parameter is approximately double that of the high-silica **MWW**-type precursor ITQ-1P (Table 1). A further indication of a structural relationship could be found in the HRTEM images, which show the presence of layers similar to those in **MWW**-type materials

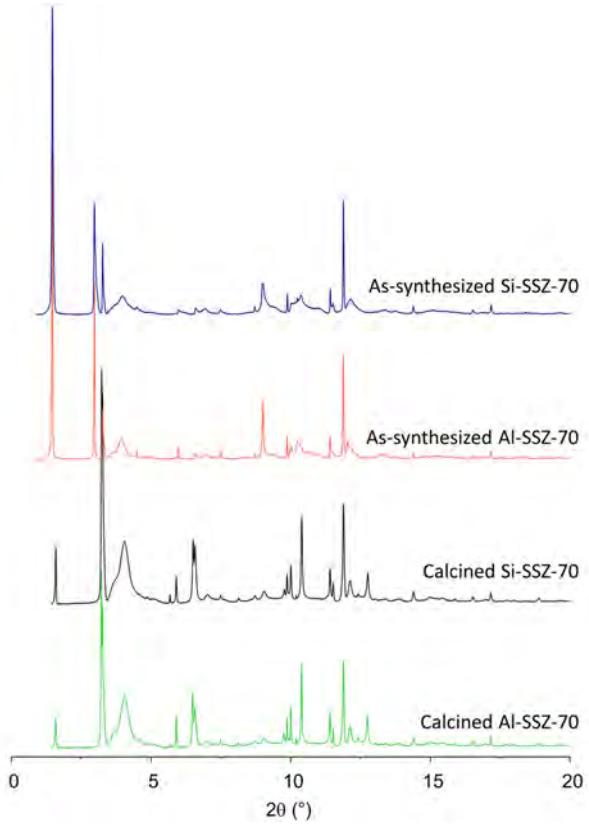

Figure 3. (Top to bottom) Synchrotron XRPD data collected on as-synthesized Si-SSZ-70 and Al-SSZ-70 and calcined Si-SSZ-70 and Al-SSZ-70.

Table 1. Unit Cell Parameters of the As-Synthesized and Calcined Versions of Si-SSZ-70 and ITQ-1

	space group	a (Å)	c (Å)	vol. (Å^3)
ITQ-1P (as-synth)20	$P6/mmm$	14.2091	27.4877	4806.39
ITQ-1 (calcined)19	$P6/mmm$	14.2081	24.9450	4361.00
SSZ-70 (as-synth)	$P6_3/mmc$	14.223	53.786	9422.85
SSZ-70 (calcined)	$P6_3/mmc$	14.227	49.806	8730.64

(Figure 4a) and also reveal the irregular stacking of these layers (Figure 4b). Each layer is shifted by approximately ±1/3 in the horizontal direction (⟨110⟩) with respect to the previous one, while in the **MWW** framework structure the layers are aligned directly above one another. The dark band observed between the **MWW** layers does not necessarily indicate the presence of additional siliceous species in the interlayer region, as HRTEM images simulated using a structure model built by stacking the **MWW** layers only (overlay in Figure 4a) match the experimental image very well (Supporting Information).

We therefore turned to the XRPD data on the calcined material and were also able to index those with a hexagonal unit cell ($P6_3/mmc$, a = 14.227 Å, c = 49.806 Å). The contraction of approximately 4 Å in the c direction with respect to the as-synthesized form is similar to that found in ITQ-1 (Table 1), supporting the hypothesis that SSZ-70 does indeed consist of silicate layers that condense upon calcination. The broadened reflection around 4° 2θ (013) in the XRPD patterns of both the as-synthesized and the calcined materials (Figure 3) provides clear evidence that stacking disorder is present in SSZ-70 and that this disorder persists through calcination. Unfortunately, this also prevents its structure from being determined and

DOI: 10.1021/jacs.7b08810
J. Am. Chem. Soc. 2017, 139, 16803−16812

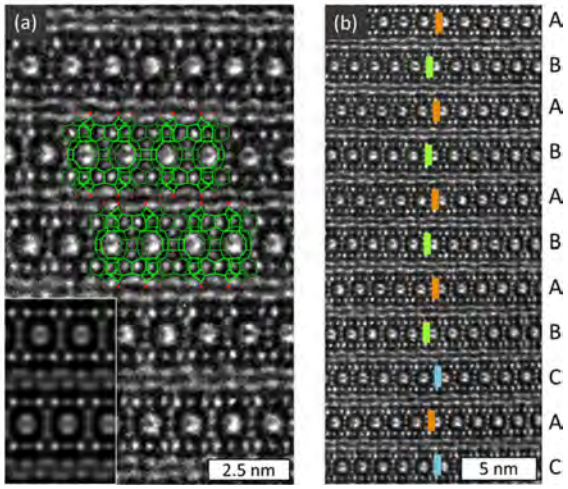

Figure 4. HRTEM images along the *b*-axis of as-synthesized Al-SSZ-70. (a) Image with an outline of the **MWW**-layers overlaid. Each layer is shifted by ±1/3 along ⟨100⟩ with respect to the neighboring one. The inset (lower left) shows an image simulated from the outlined structural model. (b) Larger area with a schematic description of the ABC stacking disorder. The colored lines indicate the positions of the 10-ring pore.

refined in a conventional manner. Therefore, we first looked at what is known about its ordered **MWW**-type counterpart, ITQ-1.[16]

Relationship between SSZ-70 and ITQ-1. ITQ-1P is the layered precursor to the pure silica **MWW**-type material ITQ-1, which is formed only upon calcination, when the layers condense to form an ordered three-dimensional framework (Figure 5a). The relationship between as-synthesized and calcined SSZ-70 is similar. Solid-state ^{29}Si MAS NMR spectra reported for high-silica ITQ-1P show an intense signal (ca. 30% of the total ^{29}Si signal intensity) around −95 ppm, which is characteristic of Q^3 (Si with three O−Si linkages) silicate species.[16] Camblor and co-workers showed that this peak disappears completely upon calcination, consistent with a condensation of the silicate layers. Structure refinement using XRPD data confirmed that calcined ITQ-1 has low defect concentrations and a three-dimensional, fully 4-connected framework structure. In the same study, they claimed that the distribution of Q^3 Si sites in the precursor is not random. Indeed, in the follow-up study by Njo,[45] the Q^3 sites in ITQ-1P were assigned to Si1 silanol groups protruding from the surface of the layer (Figure 5c), and the best XRPD agreement values were obtained with partial occupation (occupancy = 0.5) of these Si sites. It should be noted that the *c* lattice parameter of ITQ-1P is too small to accommodate the simultaneous occupation of opposing Si1 silanol groups in adjacent layers, so an occupancy of 0.5 also makes chemical sense. An attempt was made to determine the nature of the species in the interlayer region of the precursor, in order to better understand what happens during calcination, but the results were inconclusive.

Initial Structural Model of Calcined SSZ-70. Conventional ^{29}Si MAS NMR spectra for as-synthesized and calcined SSZ-70 have been reported as part of the study by Archer and co-workers.[14] The spectrum for as-synthesized SSZ-70 is very similar to that of ITQ-1P. The ^{29}Si signal at −95 ppm present in ITQ-1P can also be found in the spectrum of as-synthesized Si-SSZ-70, with the key difference that it does not disappear

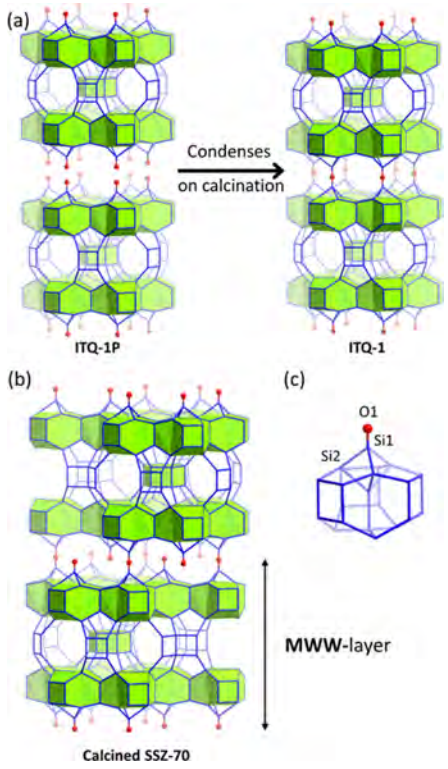

Figure 5. (a) Schematic representation of ITQ-1P and its transformation into ITQ-1 (**MWW**) upon calcination. (b) Schematic representation of the structure of calcined SSZ-70, showing the **MWW** layers. (c) Building unit of **MWW** showing the terminal −SiOH group responsible for linking the layers.

completely upon calcination. Based on the intensity of this peak, the population of Q^3 Si sites for as-synthesized SSZ-70 was estimated to be approximately 10%, and after calcination, 5%. This indicates that approximately half of the terminal −SiOH species condense on calcination to form Q^4 Si species that connect the **MWW** layers.

With the constraint that only half of the terminal Si atoms in adjacent **MWW** layers need to align with one another for condensation, a model could be built for calcined SSZ-70 (Figure 5b). In this model, which we refer to as model 1, half of the interlayer Si atoms are connected to form an oxygen bridge to the neighboring layer, while the other half point into the pocket of that layer. The coordinates for the atoms in the second layer are $x + 1/3$, $y + 2/3$ or $x + 2/3$, $y + 1/3$ where x and y are those for the first layer (Figure 6). This model fits well with the disorder observed in the HRTEM images of the as-synthesized material because there are two possible positions for each layer, just as in the ABC-type stacking of spheres.

The interatomic distances in the model were optimized using distance least-squares,[46] and the program DIFFaX[47] was used to simulate the stacking disorder in calcined SSZ-70. Three identical **MWW** layers (A, B, and C) were introduced into the program with a *c*-parameter (stacking distance) of 24.903 Å and the layer shifts described above. There was no indication in the HRTEM images of AA stacking (**MWW** structure), so each shift was assumed to have equal probability. In essence, A → B and A → C have equal probabilities (P(A → B) = P(A → C) = 0.5), but A → A is forbidden (P(A → A) = 0). The resulting simulated pattern corresponds very well to the observed one and accurately simulates the observed broadening of the reflections (Figure S1). However, a shoulder to the left of the

DOI: 10.1021/jacs.7b08810
J. Am. Chem. Soc. 2017, 139, 16803−16812

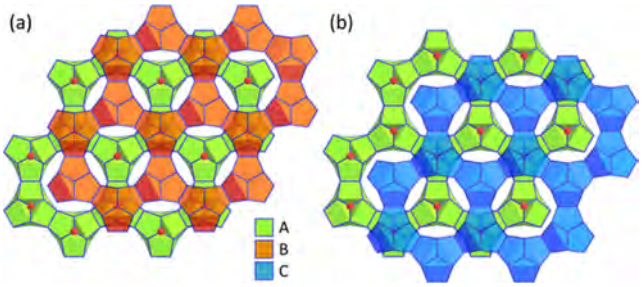

Figure 6. Schematic representation of the two possible stacking arrangements of the **MWW** layers in SSZ-70. The layers can be viewed as a hexagonal grid. Each interlayer terminal O atom (shown as red spheres) can act as a node to connect to the next layer. Only half of these O atoms in neighboring layers are used in making this connection. Viewed along the [001] direction.

broad peak at 4.0° 2θ that is observed in the measured XRPD pattern (Figure 3) is not explained by the model. Although the shoulder could arise from an **MWW**-type impurity, other features related to an AA stacking are not present. Hypothesizing that the shoulder might be linked to a higher probability of AB → A than AB → C, we carried out a new series of simulations varying the layer stacking probability from truly random (P(AB → A) = P(AB → C) = 0.5; as above), to truly ordered (P(AB → A) = 1.0, P(AB → C) = 0.0; essentially ABAB stacking). The shoulder in the simulated data becomes more pronounced as some short-range order of successive layers is introduced into the system (Figure S2). The best visual match is found for the pattern calculated with a 60% probability of short-range ABAB ordering.

Previous ^{29}Si MAS NMR results indicated the presence of approximately 3.3 Q^3 Si species per layer, but in our working model (model 1, Figure 5b) there are only two. Therefore, a second model with all of these silanol groups removed to create nests of three silanol groups (model 2) was constructed. A comparison of the two models is shown in Figure 7. The simulated diffraction pattern corresponding to model 2 (Figure S1) is very similar to that of model 1 but reproduces the observed data slightly better. The intensities of the low angle reflections are somewhat overestimated in both simulations, perhaps because residual OSDA species or adsorbed H_2O are not accounted for in the model.

Ultimately, the XRPD data cannot distinguish model 1 from model 2 definitively, so we turned to NMR to learn more. It should be noted that a third model was also considered, but it could be dismissed easily on the basis of both XRPD and NMR data (Supporting Information).

Model 1 or Model 2? By taking advantage of the large enhancements in signal sensitivity provided by DNP-enhanced MAS NMR techniques at low temperatures,[25−28] powerful 2D NMR methods can be applied to measure and understand the compositions, structures, covalent interconnectivities, and molecular-level interactions of ^{29}Si species in zeolite frameworks at natural isotopic abundance (4.7%). This precludes the need for expensive isotopic enrichment in ^{29}Si and allows 2D NMR analyses to be conducted on the same calcined Si-SSZ-70 sample as characterized by synchrotron XRPD. For example, 2D ^{29}Si{^{1}H} DNP-enhanced HETeronuclear CORrelation (HETCOR) methods selectively detect ^{29}Si species that are dipole−dipole-coupled to ^{1}H nuclei and therefore in close proximity to one another (within 0.5 nm for short contact times, e.g., 0.2 ms) and were applied to calcined Si-SSZ-70. The

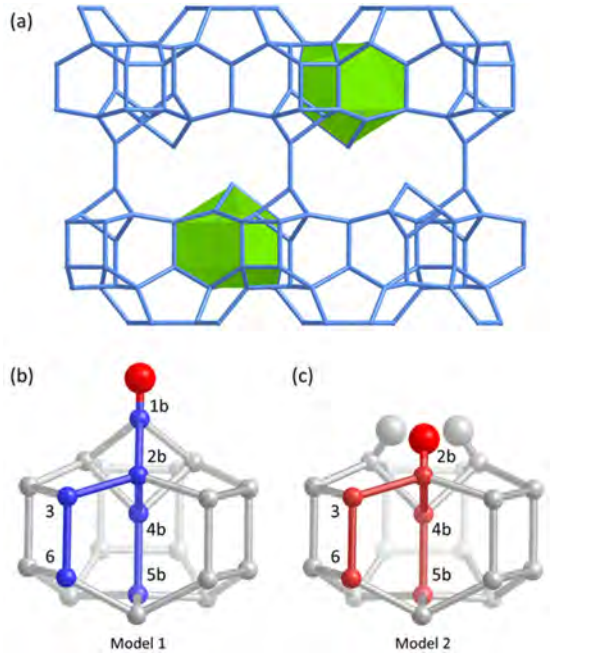

Figure 7. (a) Projection of the interlayer region of calcined Si-SSZ-70 highlighting the cages with silanol groups. (b) Cage structure for model 1 showing the four-site connectivity path with blue lines and (c) for model 2 showing the three-site connectivity path with red lines.

resulting spectra are plotted as 2D frequency contour maps with normalized ^{1}H and ^{29}Si chemical shift axes such as in Figure 8. At very short contact times (0.2 ms), the 2D ^{29}Si{^{1}H} DNP-HETCOR spectrum exhibits ^{29}Si signals at −99 ppm from interlayer ^{29}Si Q^3 silanol species that are correlated with ^{1}H signal intensities at 3.0 and 8.8 ppm from isolated and

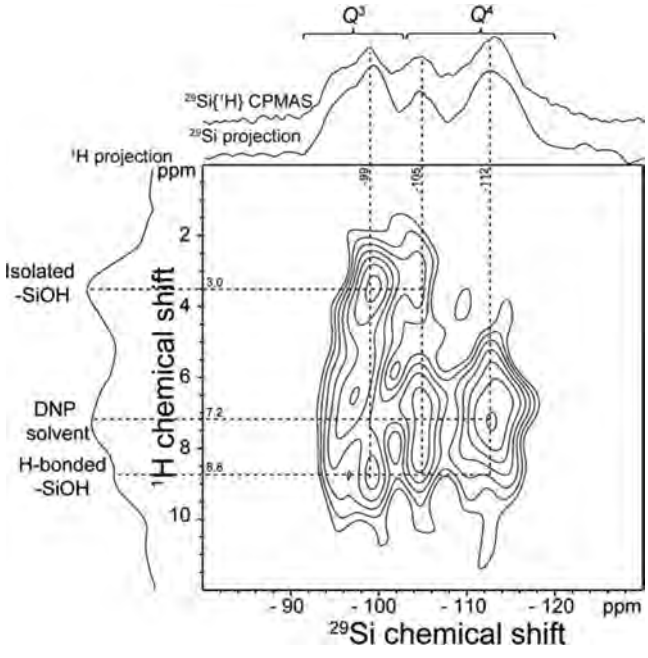

Figure 8. Solid-state DNP-enhanced 2D ^{29}Si{^{1}H} dipolar-mediated HETCOR spectrum of calcined Si-SSZ-70 with a contact times of 0.2 ms. A 1D ^{29}Si{^{1}H} DNP-CPMAS spectrum acquired under the same conditions is shown along the horizontal axis for comparison with the 1D projection of the 2D spectrum.

DOI: 10.1021/jacs.7b08810
J. Am. Chem. Soc. 2017, 139, 16803−16812

strongly H-bonded −SiOH moieties, respectively. The former correlated intensities are consistent with the isolated silanol groups in model 1 and the latter with the silanol nests in model 2. Additional partially resolved ^{29}Si signals at −105 and −112 ppm arise from Q^4 species in the zeolite framework. The broad correlated intensity at 7.0 ppm in the ^{1}H dimension with ^{29}Si signals from −94 to −118 ppm arises from DNP solvent interactions in the zeolite nanopores. At longer contact times, the ^{29}Si signals from both Q^3 and Q^4 ^{29}Si species are all correlated with all ^{1}H signals, which reveals that the different types of −SiOH moieties are commingled over nanoscale dimensions (Figure S3). More details about the DNP-HETCOR analyses can be found in Figures S3−S5.

Though the different candidate structures in Figure 7 are very similar, they are distinguished by the different local bonding environments associated with their respective interlayer Q^3 silanol moieties. In particular, the Q^3 Si sites are covalently linked to three equivalent Q^4 Si sites (Si2b) in model 1 and to two different Q^4 Si sites (Si3 and Si4b) in model 2. Therefore, the different interlayer surface structures are expected to lead to distinct pairs of correlated intensities in 2D *J*-mediated ^{29}Si{^{29}Si} NMR spectra. Importantly, such spectra resolve and correlate inhomogeneously broadened ^{29}Si signals, which strongly overlap in 1D ^{29}Si spectra. Correlated pairs of ^{29}Si signal intensity unambiguously establish the covalent ^{29}Si−O−^{29}Si connectivities of nearest neighbor Q^3 and Q^4 ^{29}Si sites, which were previously unfeasible to measure for natural abundance ^{29}Si (4.7%) materials. A DNP-enhanced 2D ^{29}Si{^{29}Si} dipolar-mediated (through-space) NMR correlation spectrum of calcined Si-SSZ-70 was also acquired, though it contains contributions from *next*-nearest neighbor sites as well, which complicate the analysis (Figure S7).

The sensitivity enhancements provided by DNP-NMR enabled acquisition of the 2D *J*-mediated ^{29}Si{^{29}Si} correlation spectrum shown in Figure 9a, which resolves multiple intensity correlations that correspond to covalent connectivities between distinct Q^3 and Q^4 ^{29}Si framework species. The spectrum is dominated by broad ^{29}Si signal intensity straddling the diagonal from −110 to −121 ppm, which arises from overlapping signals associated with covalently bonded ^{29}Si−O-^{29} moieties that are fully cross-linked and can be assigned to Q^4 ^{29}Si sites in the **MWW** layers. Their shift values are consistent with (1) previous results on similar zeolites,[16,48] (2) chemical shieldings calculated using the proposed models for calcined zeolite Si-SSZ-70 and well-established semiempirical relationships,[49,50] and (3) signals detected in a similar DNP-enhanced 2D ^{29}Si{^{29}Si} *J*-mediated spectrum of calcined ITQ-1 (Figure S8). While the signals are broadened by interactions with frozen TCE solvent molecules in the zeolite nanopores, the resolution provided by the 2D spectrum is nevertheless sufficient to resolve pairs of correlated signal intensity that arise from the covalent interconnectivities of different framework Q^4 sites. These signals are tabulated and analyzed in detail in Figure S9 and Table S1.

Of most interest here are the pairs of correlated ^{29}Si signals associated with the Q^3 −SiOH moieties that are not present in **MWW**-type zeolites and that enable the candidate models for calcined SSZ-70 to be distinguished. While the ^{29}Si signals from the Q^3 species overlap in the range −94 to −101 ppm in the conventional 1D ^{29}Si MAS spectrum (Figure 9b), they are resolved in the 2D DNP-enhanced ^{29}Si{^{29}Si} *J*-mediated spectrum. On the basis of the analysis of the ^{29}Si DNP-NMR spectra of calcined ITQ-1 (Figure S8), ^{29}Si signals in the −105

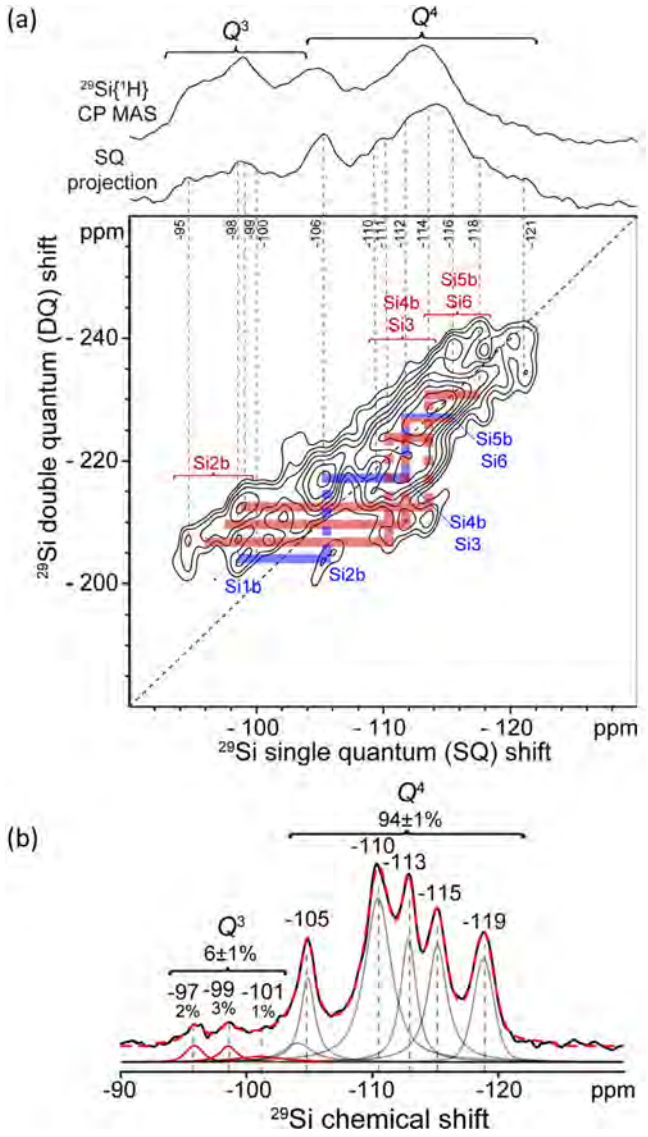

Figure 9. (a) Solid-state DNP-enhanced 2D ^{29}Si{^{29}Si} *J*-mediated correlation spectrum of calcined Si-SSZ-70. A 1D ^{29}Si{^{1}H} DNP-CPMAS spectrum acquired under the same conditions is shown along the vertical axis for comparison with the 1D projection of the 2D spectrum. 2D intensity correlations associated with covalent connectivities of Q^3 and Q^4 ^{29}Si species that are consistent with models 1 and 2 are indicated by blue and red lines, respectively. (b) Solid-state quantitative 1D single-pulse ^{29}Si MAS NMR spectrum acquired at 11.7 T, 298 K, and 10 kHz MAS. The simulated spectrum is the dotted red line with the fit deconvolution offset below.

to −106 ppm range are assigned to Si2b Q^4 sites in model 1, while ^{29}Si signals from Si4b and Si3 sites overlap in the −109 to −113 ppm range. In the 2D spectrum in Figure 9a, the broad ^{29}Si signals in the Q^3 range (−98 to −100 ppm) are correlated (lower blue line) with signals that can be attributed to Q^4 Si2b sites in model 1. These Si2b ^{29}Si signals are themselves correlated with the broad intensity maximum at ca. −112 ppm attributed to Si4b and Si3 sites, and these in turn with intensity at ca. −116 ppm attributed to Si5b and Si6 sites. These three pairs of ^{29}Si intensity correlations are indicated by the blue lines in Figure 9a. In model 1, there are two paths of three Si−O−Si covalent linkages connecting the Q^3 Si1b silanol moieties at the interlayer surface with the Q^4 species at the surface of the

DOI: 10.1021/jacs.7b08810
J. Am. Chem. Soc. 2017, 139, 16803−16812

channel system within the layer (Si1b−O−Si2b−O−Si4b−O−Si5b and Si1b−O−Si2b−O−Si3−O−Si6). These relatively long four-site connectivity paths are shown in blue in Figure 7b.

However, there are further ^{29}Si intensity correlations from distinct covalently linked Q^3 and Q^4 moieties in Figure 9a that cannot be assigned to model 1 and are instead consistent with model 2. Specifically, partially resolved Q^3 ^{29}Si signals in the range −94 to −99 ppm are each correlated with intensity from −110 to −114 ppm in the Q^4 region of the spectrum that can be assigned to Si4b and Si3 sites (lower red lines in Figure 9a). These in turn are correlated with ^{29}Si signals in the range −114 to −118 ppm (upper red lines), which are assigned to overlapping signals from sites Si5b and Si6. These results reflect the two shorter Si−O−Si covalent interconnectivity paths between the Q^3 S2b silanol moieties and Q^4 sites at the intralayer channel surfaces (Si2b−O−Si4b−O−Si5b and Si2b−O−Si3−O−Si6). These relatively short three-site connectivity paths are consistent with model 2 and shown in red in Figure 7c.

The high signal sensitivity and spectral resolution of the 2D DNP-enhanced *J*-mediated ^{29}Si{^{29}Si} spectrum of calcined zeolite Si-SSZ-70 thus provide direct evidence of the presence of two distinct types of Q^3 silanol species in the material. One has covalent connectivities that are consistent with model 1 and the other with model 2. Neither model alone is consistent with all of the observed connectivities. Although the ^{29}Si signals overlap in the quantitative 1D single-pulse ^{29}Si MAS NMR spectrum in Figure 9b, the enhanced resolution of the 2D DNP-NMR spectrum enables the positions and line widths of partially resolved ^{29}Si signals in the single-pulse spectrum to be deconvoluted with confidence and their relative integrated intensities and site populations quantified. Noting that the percentages of Q^3 sites in models 1 and 2 are distinct (3% and 9%, respectively), we estimate that 50 ± 10% of the calcined Si-SSZ-70 material is structurally consistent with model 1 and 50 ± 10% with model 2. The estimated uncertainties arise from the low absolute quantities of Q^3 moieties in the material (ca. 6 ± 1%) and the ^{29}Si signal fits.

Structure of Calcined SSZ-70. The framework structure of calcined SSZ-70 can then be described as a polytype of **MWW**, with an almost random ABC-type stacking of **MWW**layers to create the framework shown in Figure 5. Each layer is translated by $(x + 1/3, y + 2/3)$ or $(x + 2/3, y + 1/3)$ with respect to the previous one, with a probability of 50% for either translation. Our simulations show that some short-range ordering, where ABA has a slightly higher chance of occurring (60%) than ABC (40%), is present. The isolated silanol groups protruding into the interlayer space and pointing toward the pocket of the adjacent layer in Figure 5b are only present 50% of the time. When they are absent, a nest of three silanol groups is present (Figure 7). A model for calcined Si-SSZ-70 with these stacking probabilities and a 50% occupancy of the Si1b and O1b sites results in a diffraction pattern that shows good agreement with the observed data (Figure 10). The average structure can be described in $P6_3/mmc$ symmetry with a = 14.227 Å and c = 49.806 Å as an ABAB stacking of **MWW** layers. Prominent examples in zeolite structures with similar stacking disorder include the ABC-6 family[51] and the **FAU**/**EMT** systems.[52]

Despite the disorder, the regions between the layers are topologically identical. The layers are connected via widely spaced bridging oxygen atoms, forming elongated 14-ring windows lying along ⟨110⟩, with free dimensions of 4.0 Å × 11.5 Å (Figure 11a, b). The terminal SiOH groups in models 1 and 2 act as additional obstacles for diffusion through the channels. These pores form a 2D channel system between the **MWW** layers that is very different from that in the **MWW** framework structure. In calcined Si-SSZ-70, there are only half as many oxygen bridges between the layers as in ITQ-1 (**MWW**). The other half are replaced by silanol groups (either isolated or nests of three) opposite the 12-ring pockets of the adjacent layer. From the NMR results, we estimate that there are approximately equal numbers of the two types of silanol species (Figure 11c). This corresponds to four −SiOH groups per **MWW** layer in the unit cell, in good agreement with the value of 3.3 estimated in earlier work.[14]

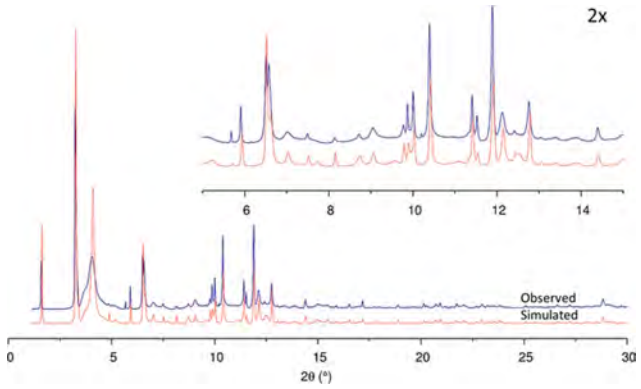

Figure 10. Observed (blue) and simulated (red) pattern generated by DIFFaX for calcined Si-SSZ-70, corresponding to a 50/50 mixture of models 1 and 2 with a 60% chance of short-range ABAB ordering of the layers.

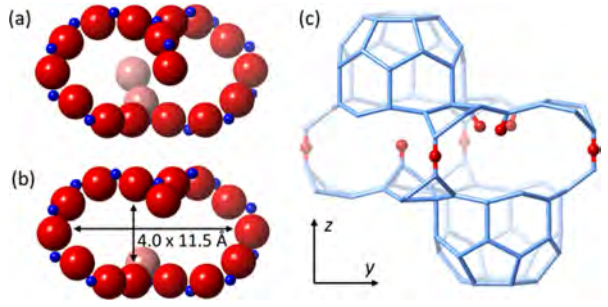

Figure 11. Effective pore opening of the 14-ring window for (a) model 1 and (b) model 2. The van der Waals radius of O (1.35 Å) has been taken into account in calculating the distances. (c) Schematic representation of the interlayer region along ⟨110⟩ showing the two possible arrangements. The terminal and layer-bridging O atoms are shown in red, but the others have been omitted for clarity.

Catalytic Aspects. With this greater insight into the organization and distinction of silanol groups at the SSZ-70 interlayer surfaces, new opportunities and challenges for the development of newer catalysts based upon SSZ-70 arise. The reduced number of potential linkages between **MWW** layers in the as-synthesized form of SSZ-70 (compared with **MWW**-type materials) may explain why it is such a good candidate for delamination using milder nonaqueous treatment conditions. A high degree of externally exposed surface area is achieved while leaving the intrinsic structure intact. Even without the detailed understanding presented here, Katz and co-workers have already produced some exceptional Lewis acid catalysts based on SSZ-70 by inserting tin[53] or titanium[54] (in place of boron in

DOI: 10.1021/jacs.7b08810
J. Am. Chem. Soc. 2017, 139, 16803−16812

B-SSZ-70) into the cups on the interlayer surface. The latter catalyst seems to exceed commercial materials in performance for partial oxidation reactions.

With the structural details of Si-SSZ-70 that have been learned in this study, new possibilities for enhancing the performance of a class of catalysts that are already active and performing well can be envisaged. Indeed, Aigner et al. recently showed that the delamination procedure for Ti-SSZ-70 materials has a significant effect on catalytic performance.[55] Another question is whether the location of the substituting heteroatom can be controlled differentially to create single-site catalysts with a variation in the environment around the site.

Further Points of Discussion. Recently, the structure of a new zeolite, ECNU-5, synthesized by rapid dissolution−recrystallization of an **MWW**-type material was reported.[56] We were surprised to discover that the powder pattern of ECNU-5 closely resembles that of calcined Si-SSZ-70. However, the structure of ECNU-5 was described as an intergrowth of two polymorphs with ABAB and ABCABC stackings of **MWW** layers. We believe that our model for calcined SSZ-70 with an almost random stacking sequence fits the data for ECNU-5 better than the intergrowth model. This is most noticeable in the 12−13° 2θ region in the XRPD pattern of ECNU-5, where it exhibits two small reflections. With the intergrowth model, one of these is absent, while the other is greatly overestimated. Both are present in the simulated data for the disordered model for calcined SSZ-70 (~6° 2θ in Figure 10) and have intensities comparable to the observed data. For completeness, we also compared the ECNU-5 intergrowth model with our data, but the match was much worse than with the simpler random stacking model.

A wide variety of layer packing possibilities in the **MWW** family has been discovered.[57] However, one with lateral disorder was missing until ECNU-5 and now SSZ-70 were reported. Roth and Dorset have classified each type of layer stacking (conventional, layered ordered/disordered, delaminated, swollen/pillared), and they showed how each type can be identified with a few unique features in the low angle region of the XRPD diffraction patterns. To extend their classification, the diffraction pattern of SSZ-70 can be distinguished clearly on the basis of the characteristic broad reflection at 4.0° 2θ in Figure 3 (d = 10.0 Å) or 8.8° 2θ with a laboratory instrument (Cu Kα radiation).

CONCLUSION

For the determination of the structures of complex polycrystalline materials, conventional methods are rarely sufficient, so information from different sources must be combined.[58−69] This process is much like solving a puzzle, where data and constraints over multiple length scales must be analyzed to establish a structure (or distribution of structures) that is consistent with all data. Sometimes such data simply provides independently corroborative information, but for SSZ-70, the HRTEM images, synchrotron XRPD data, and DNP-enhanced 2D NMR spectra, each provided crucial and complementary insights. Specifically, the HRTEM images provided evidence that the framework structure of calcined Si-SSZ-70 is a polytype of **MWW** consisting of laterally displaced **MWW** layers, the initial XRPD data analysis yielded the unit cell and space-group symmetry, and 1D ^{29}Si MAS NMR data indicated that only half of the silanol groups condensed upon calcination. With this information, it was possible to build an initial model of the structure. A more accurate description of the disordered stacking of the **MWW**-layers could then be derived from the XRPD data. Finally, the combined sensitivity and resolution of the DNP-enhanced 2D ^{29}Si{^{1}H} and ^{29}Si{^{29}Si} NMR analyses established the types and bonding environments of terminal −SiOH groups at the interlayer surfaces. Three state-of-the-art characterization techniques were used to probe different structural aspects of calcined SSZ-70, ranging from the long-range average structure (>500 nm) to short-range stacking sequences (ca. 50 nm) to local atomic-level compositions and structures (<1 nm). The combination is particularly well suited to the investigation of materials with complex partially disordered structures that cannot be resolved with conventional X-ray diffraction analysis alone.

Obtaining detailed structural information for zeolites at natural isotopic abundance of ^{29}Si (4.7%) from solid-state ^{29}Si NMR has previously been challenging because the low sensitivity of conventional methods made it unfeasible to determine the covalent ^{29}Si−O−^{29}Si interconnectivities within the framework. However, by exploiting DNP-enhanced NMR techniques, which dramatically increase ^{29}Si NMR signal sensitivity, the interconnectivities and the relative proximities of different framework silicate sites have been established, even for natural abundance ^{29}Si in calcined zeolite Si-SSZ-70.

The deeper understanding of the structural details of SSZ-70 realized in this study are expected to enable further development toward new single-site selective heterogeneous catalysts via carefully controlled chemical modification.

ASSOCIATED CONTENT

Supporting Information

The Supporting Information is available free of charge on the ACS Publications website at DOI: 10.1021/jacs.7b08810.

Idealized structural model for calcined SSZ-70 (CIF)
Detailed descriptions of the 2D DNP-enhanced NMR analyses and DiFFaX simulations (PDF)

AUTHOR INFORMATION

Corresponding Author

*stef.smeets@mmk.su.se

ORCID

Stef Smeets: 0000-0002-5413-9038
Xiaodong Zou: 0000-0001-6748-6656
Bradley F. Chmelka: 0000-0002-4450-6949

Present Address

⊗(M.F.H.) Johnson Matthey Technology Centre, Chilton P.O. Box 1, Belasis Avenue, Billingham TS23 1LB, U.K..

Notes

The authors declare no competing financial interest.

ACKNOWLEDGMENTS

We thank Antonio Cervellino and Nicola Casati for their assistance with the powder diffraction measurements on the Materials Science Beamline at the SLS in Villigen, Switzerland. The work at ETH was funded in part by the Swiss National Science Foundation. The work at UCSB was supported in part by the U.S. National Science Foundation under Grant No. DMR-1429710 and by the Chevron Energy Technology Company (Richmond, CA). The NMR measurements made use of shared facilities of the UCSB MRSEC (NSF DMR 1720256), a member of the Materials Research Facilities Network (www.mrfn.org). The work at SU was funded in part

DOI: 10.1021/jacs.7b08810
J. Am. Chem. Soc. 2017, 139, 16803−16812

by the Knut and Alice Wallenberg foundation through a grant for purchasing the TEMs and Project Grant 3DEM-NATUR and by the Swedish Research Council (VR) through the MATsynCELL project.

REFERENCES

(1) Zones, S. I. *Microporous Mesoporous Mater.* **2011**, *144*, 1−8.
(2) Zones, S. I.; Chen, C. Y.; Benin, A.; Hwang, S.-J. *J. Catal.* **2013**, *308*, 213−225.
(3) Gounder, R.; Iglesia, E. *Angew. Chem., Int. Ed.* **2010**, *49* (4), 808−811.
(4) Corma, A. *J. Catal.* **2003**, *216* (1−2), 298−312.
(5) Cheung, P.; Bhan, A.; Sunley, G. J.; Iglesia, E. *Angew. Chem., Int. Ed.* **2006**, *45* (10), 1617−1620.
(6) Boronat, M.; Martínez-Sánchez, C.; Law, D.; Corma, A. *J. Am. Chem. Soc.* **2008**, *130* (48), 16316−16323.
(7) Zones, S. I.; Benin, A.; Hwang, S.-J.; Xie, D.; Elomari, S.; Hsieh, M.-F. *J. Am. Chem. Soc.* **2014**, *136* (4), 1462−1471.
(8) Gallego, E. M.; Portilla, M. T.; Paris, C.; León-Escamilla, A.; Boronat, M.; Moliner, M.; Corma, A. *Science* **2017**, *355* (6329), 1051−1054.
(9) Zones, S. I.; Hwang, S.-J. *Microporous Mesoporous Mater.* **2011**, *146* (1), 48−56.
(10) Zones, S. I. *Zeolites* **1989**, *9* (6), 458−467.
(11) Zones, S. I.; Burton, A. W. Molecular sieve SSZ-70 composition of matter and synthesis thereof. US7108843 B2, Sep 19, 2006.
(12) Archer, R. H.; Zones, S. I.; Davis, M. E. *Microporous Mesoporous Mater.* **2010**, *130* (1−3), 255−265.
(13) Leonowicz, M. E.; Lawton, J. A.; Lawton, S. L.; Rubin, M. K. *Science* **1994**, *264* (5167), 1910−1913.
(14) Archer, R. H.; Carpenter, J. R.; Hwang, S.-J.; Burton, A. W.; Chen, C.-Y.; Zones, S. I.; Davis, M. E. *Chem. Mater.* **2010**, *22* (8), 2563−2572.
(15) Chu, P.; Landis, M. E.; Le, Q. N. Production of ethylbenzene. US5334795 A, Aug 2, 1994.
(16) Camblor, M. A.; Corma, A.; Díaz-Cabañas, M.-J.; Baerlocher, C. *J. Phys. Chem. B* **1998**, *102* (1), 44−51.
(17) Zones, S. I.; Holtermann, D. I.; Innes, R. A.; Pecoraro, T. A.; Santilli, D. S.; Ziemer, J. N. Zeolite SSZ-25. US4826667 A, May 2, 1989.
(18) Runnebaum, R. C.; Ouyang, X.; Edsinga, J. A.; Rea, T.; Arslan, I.; Hwang, S.-J.; Zones, S. I.; Katz, A. *ACS Catal.* **2014**, *4* (7), 2364−2368.
(19) Zones, S. I.; Harris, T. V. *Microporous Mesoporous Mater.* **2000**, *35*−*36*, 31−46.
(20) Ouyang, X.; Hwang, S.-J.; Runnebaum, R. C.; Xie, D.; Wanglee, Y.-J.; Rea, T.; Zones, S. I.; Katz, A. *J. Am. Chem. Soc.* **2014**, *136* (4), 1449−1461.
(21) Ogino, I.; Nigra, M. M.; Hwang, S.-J.; Ha, J.-M.; Rea, T.; Zones, S. I.; Katz, A. *J. Am. Chem. Soc.* **2011**, *133* (10), 3288−3291.
(22) Maheshwari, S.; Martínez, C.; Teresa Portilla, M.; Llopis, F. J.; Corma, A.; Tsapatsis, M. *J. Catal.* **2010**, *272* (2), 298−308.
(23) Bergamaschi, A.; Cervellino, A.; Dinapoli, R.; Gozzo, F.; Henrich, B.; Johnson, I.; Kraft, P.; Mozzanica, A.; Schmitt, B.; Shi, X. *J. Synchrotron Radiat.* **2010**, *17* (5), 653−668.
(24) Xie, D.; McCusker, L. B.; Baerlocher, C.; Zones, S. I.; Wan, W.; Zou, X. *J. Am. Chem. Soc.* **2013**, *135* (28), 10519−10524.
(25) Maly, T.; Debelouchina, G. T.; Bajaj, V. S.; Hu, K.-N.; Joo, C.-G.; Mak-Jurkauskas, M. L.; Sirigiri, J. R.; van der Wel, P. C. A.; Herzfeld, J.; Temkin, R. J.; Griffin, R. G. *J. Chem. Phys.* **2008**, *128* (5), 052211.
(26) Lesage, A.; Lelli, M.; Gajan, D.; Caporini, M. A.; Vitzthum, V.; Miéville, P.; Alauzun, J.; Roussey, A.; Thieuleux, C.; Mehdi, A.; Bodenhausen, G.; Coperet, C.; Emsley, L. *J. Am. Chem. Soc.* **2010**, *132* (44), 15459−15461.
(27) Ni, Q. Z.; Daviso, E.; Can, T. V.; Markhasin, E.; Jawla, S. K.; Swager, T. M.; Temkin, R. J.; Herzfeld, J.; Griffin, R. G. *Acc. Chem. Res.* **2013**, *46* (9), 1933−1941.
(28) Rossini, A. J.; Zagdoun, A.; Lelli, M.; Lesage, A.; Copéret, C.; Emsley, L. *Acc. Chem. Res.* **2013**, *46* (9), 1942−1951.
(29) Perras, F. A.; Kobayashi, T.; Pruski, M. *J. Am. Chem. Soc.* **2015**, *137* (26), 8336−8339.
(30) Perras, F. A.; Padmos, J. D.; Johnson, R. L.; Wang, L.-L.; Schwartz, T. J.; Kobayashi, T.; Horton, J. H.; Dumesic, J. A.; Shanks, B. H.; Johnson, D. D.; Pruski, M. *J. Am. Chem. Soc.* **2017**, *139* (7), 2702−2709.
(31) Copéret, C.; Liao, W.-C.; Gordon, C. P.; Ong, T.-C. *J. Am. Chem. Soc.* **2017**, *139* (31), 10588−10596.
(32) Kobayashi, T.; Singappuli-Arachchige, D.; Wang, Z.; Slowing, I.; Pruski, M. *Phys. Chem. Chem. Phys.* **2017**, *19* (3), 1781−1789.
(33) Lee, D.; Monin, G.; Duong, N. T.; Lopez, I. Z.; Bardet, M.; Mareau, V.; Gonon, L.; De Paëpe, G. *J. Am. Chem. Soc.* **2014**, *136* (39), 13781−13788.
(34) Wolf, P.; Valla, M.; Rossini, A. J.; Comas-Vives, A.; Núñez-Zarur, F.; Malaman, B.; Lesage, A.; Emsley, L.; Copéret, C.; Hermans, I. *Angew. Chem., Int. Ed.* **2014**, *53* (38), 10179−10183.
(35) Gunther, W. R.; Michaelis, V. K.; Caporini, M. A.; Griffin, R. G.; Román-Leshkov, Y. *J. Am. Chem. Soc.* **2014**, *136* (17), 6219−6222.
(36) Sangodkar, R. P.; Smith, B. J.; Gajan, D.; Rossini, A. J.; Roberts, L. R.; Funkhouser, G. P.; Lesage, A.; Emsley, L.; Chmelka, B. F. *J. Am. Chem. Soc.* **2015**, *137* (25), 8096−8112.
(37) Wolf, P.; Valla, M.; Núñez-Zarur, F.; Comas-Vives, A.; Rossini, A. J.; Firth, C.; Kallas, H.; Lesage, A.; Emsley, L.; Copéret, C.; Hermans, I. *ACS Catal.* **2016**, *6* (7), 4047−4063.
(38) Berkson, Z. J.; Messinger, R. J.; Na, K.; Seo, Y.; Ryoo, R.; Chmelka, B. F. *Angew. Chem., Int. Ed.* **2017**, *56* (19), 5164−5169.
(39) Zagdoun, A.; Casano, G.; Ouari, O.; Schwarzwälder, M.; Rossini, A. J.; Aussenac, F.; Yulikov, M.; Jeschke, G.; Copéret, C.; Lesage, A.; Tordo, P.; Emsley, L. *J. Am. Chem. Soc.* **2013**, *135* (34), 12790−12797.
(40) Zagdoun, A.; Rossini, A. J.; Gajan, D.; Bourdolle, A.; Ouari, O.; Rosay, M.; Maas, W. E.; Tordo, P.; Lelli, M.; Emsley, L.; Lesage, A.; Copéret, C. *Chem. Commun.* **2012**, *48* (5), 654−656.
(41) Lesage, A.; Bardet, M.; Emsley, L. *J. Am. Chem. Soc.* **1999**, *121* (47), 10987−10993.
(42) Cadars, S.; Mifsud, N.; Lesage, A.; Epping, J. D.; Hedin, N.; Chmelka, B. F.; Emsley, L. *J. Phys. Chem. C* **2008**, *112* (25), 9145−9154.
(43) Elena, B.; de Paëpe, G.; Emsley, L. *Chem. Phys. Lett.* **2004**, *398* (4), 532−538.
(44) Fung, B. M.; Khitrin, A. K.; Ermolaev, K. *J. Magn. Reson.* **2000**, *142* (1), 97−101.
(45) Njo, S. L. *Computational Chemistry Approaches to Zeolite Frameworks and their Interactions with Structure Directing Agents*. PhD Thesis, TU Delft, The Netherlands, 1998.
(46) Baerlocher, C.; Hepp, A.; Meier, W. M. *DLS-76*, 1976.
(47) Treacy, M. M. J.; Newsam, J. M.; Deem, M. W. *Proc. R. Soc. London, Ser. A* **1991**, *433* (1889), 499−520.
(48) Camblor, M. A.; Corell, C.; Corma, A.; Díaz-Cabañas, M.-J.; Nicolopoulos, S.; González-Calbet, J. M.; Vallet-Regí, M. *Chem. Mater.* **1996**, *8* (10), 2415−2417.
(49) Lewis, J. E.; Freyhardt, C. C.; Davis, M. E. *J. Phys. Chem.* **1996**, *100* (12), 5039−5049.
(50) Brouwer, D. H.; Darton, R. J.; Morris, R. E.; Levitt, M. H. *J. Am. Chem. Soc.* **2005**, *127* (29), 10365−10370.
(51) Millward, G. R.; Ramdas, S.; Thomas, J. M. *Proc. R. Soc. London A* **1816**, *1985*, 57−71.
(52) Treacy, M. M. J.; Vaughan, D. E. W.; Strohmaier, K. G.; Newsam, J. M. *Proc. R. Soc. London, Ser. A* **1996**, *452*, 813−840.
(53) Ouyang, X.; Wanglee, Y.-J.; Hwang, S.-J.; Xie, D.; Rea, T.; Zones, S. I.; Katz, A. *Dalton Trans.* **2014**, *43*, 10417−10429.
(54) Aigner, M.; Andrés Grosso-Giordano, N.; Okrut, A.; Zones, S.; Katz, A. *React. Chem. Eng.* **2017**, DOI: 10.1039/C7RE00076F.
(55) Aigner, M.; Grosso-Giordano, N.; Schöttle, C.; Okrut, A.; Zones, S.; Katz, A. *React. Chem. Eng.* **2017**, DOI: 10.1039/C7RE00138J.
(56) Xu, L.; Ji, X.; Jiang, J.-G.; Han, L.; Che, S.; Wu, P. *Chem. Mater.* **2015**, *27*, 7852−7860.

DOI: 10.1021/jacs.7b08810
J. Am. Chem. Soc. 2017, 139, 16803−16812

(57) Roth, W. J.; Dorset, D. L. *Microporous Mesoporous Mater.* **2011**, *142*, 32−36.
(58) Fyfe, C. A.; Gies, H.; Kokotailo, G. T.; Pasztor, C.; Strobl, H.; Cox, D. E. *J. Am. Chem. Soc.* **1989**, *111*, 2470−2474.
(59) Wright, P. A.; Natarajan, S.; Thomas, J. M.; Bell, R. G.; Gai-Boyes, P. L.; Jones, R. H.; Chen, J. *Angew. Chem., Int. Ed. Engl.* **1992**, *31*, 1472−1475.
(60) Eiden-Aßmann, S.; Schneider, A. M.; Behrens, P.; Engelhardt, G.; Mändar, H.; Felsche, J. *Eur. J. Inorg. Chem.* **2001**, *2001*, 1527−1534.
(61) Cao, G.; Afeworki, M.; Kennedy, G. J.; Strohmaier, K. G.; Dorset, D. L. *Acta Crystallogr., Sect. B: Struct. Sci.* **2007**, *63*, 56−62.
(62) Wu, P.; Ruan, J.; Wang, L.; Wu, L.; Wang, Y.; Liu, Y.; Fan, W.; He, M.; Terasaki, O.; Tatsumi, T. *J. Am. Chem. Soc.* **2008**, *130*, 8178−8187.
(63) Milanesio, M.; Croce, G.; Viterbo, D.; Pastore, H. O.; Mascarenhas, A. J. dos S.; Munsignatti, E. C. de O.; Meda, L. *J. Phys. Chem. A* **2008**, *112*, 8403−8410.
(64) Sun, J.; Bonneau, C.; Cantin, A.; Corma, A.; Díaz-Cabañas, M. J.; Moliner, M.; Zhang, D.; Li, M.; Zou, X. *Nature* **2009**, *458*, 1154−1157.
(65) Inge, A. K.; Huang, S.; Chen, H.; Moraga, F.; Sun, J.; Zou, X. *Cryst. Growth Des.* **2012**, *12*, 4853−4860.
(66) Kong, X.; Deng, H.; Yan, F.; Kim, J.; Swisher, J. A.; Smit, B.; Yaghi, O. M.; Reimer, J. A. *Science* **2013**, *341*, 882−885.
(67) Smeets, S.; Xie, D.; Baerlocher, C.; McCusker, L. B.; Wan, W.; Zou, X.; Zones, S. I. *Angew. Chem., Int. Ed.* **2014**, *53*, 10398−10402.
(68) Krajnc, A.; Kos, T.; Zabukovec Logar, N.; Mali, G. *Angew. Chem., Int. Ed.* **2015**, *54*, 10535−10538.
(69) Morris, S. A.; Bignami, G. P. M.; Tian, Y.; Navarro, M.; Firth, D. S.; Čejka, J.; Wheatley, P. S.; Dawson, D. M.; Slawinski, W. A.; Wragg, D. S.; Morris, R. E.; Ashbrook, S. E. *Nat. Chem.* **2017**, *9*, 1012−1018.

DOI: 10.1021/jacs.7b08810
J. Am. Chem. Soc. 2017, 139, 16803−16812

Supporting Information for: Well-defined silanols in the structure of the calcined high-silica zeolite SSZ-70: new understanding of a successful catalytic material

Stef Smeets,*[,a,d] Zachariah J. Berkson,[b] Dan Xie,[c] Stacey I. Zones,[c] Wei Wan,[d] Xiaodong Zou,[d] Ming-Feng Hsieh,[b†] Bradley F. Chmelka,[b] Lynne B. McCusker,[a,b] Christian Baerlocher[a,b]

[a]Laboratory of Crystallography, ETH Zurich, Vladimir-Prelog-Weg 5, Zurich CH-8093, Switzerland, [b]Department of Chemical Engineering, University of California, Santa Barbara, California 93106, United States, [c]Chevron Energy Technology Company, Richmond, California 94802, United States, [d]Berzelii Center EXSELENT on Porous Materials, Department of Material and Environmental Chemistry, Stockholm University, SE-106 91 Stockholm, Sweden

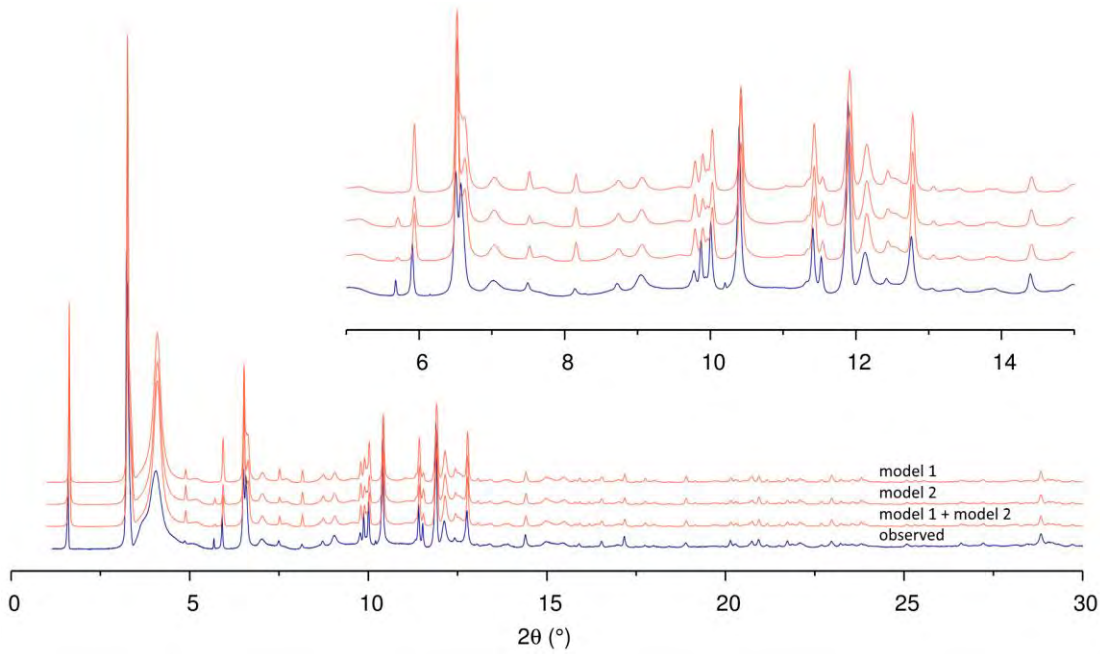

Figure S1. Observed (blue), and calculated (red) patterns corresponding to model 1, model 2, and a 50/50 mixture of models 1 and 2 generated by DIFFaX for calcined Si-SSZ-70.

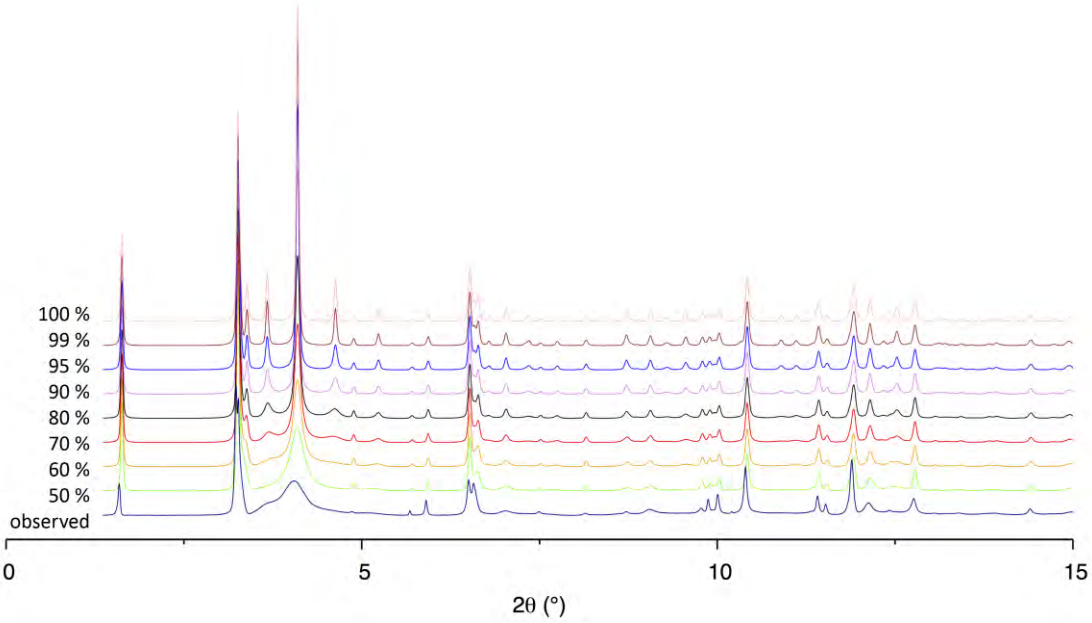

Figure S2. Comparison of the observed data for calcined Si-SSZ-70 (blue), and those calculated by *DIFFaX* with varying degrees of short-range ABAB ordering. Here, 50% corresponds to truly random stacking sequence ($\boldsymbol{P(AB \rightarrow A) = P(AB \rightarrow C) = 0.5}$), 100% corresponds to long-range ABAB ordering ($\boldsymbol{P(AB \rightarrow A) = 1.0, P(AB \rightarrow C) = 0.0}$), and anything inbetween corresponds to a preference for short-range order (*i.e.* a higher probability of the layer following AB being A rather than C).

HRTEM image simulation

A structure model of the as-synthesized SSZ-70 ($P6_3/mmc$, a = 14.223 Å, c = 53.786 Å) was built by stacking the **MWW** layers as overlaid in Figure 4a, with half of the terminal Si atoms in adjacent **MWW** layers aligned with one another. Image simulation was done using JEMS[1] for varying crystal thicknesses and defocus values. The best match between the simulation and the experimental images was found at a crystal thickness of 71 nm and a defocus value of -85 nm.

Sensitivity enhancements provided by DNP-NMR

DNP-enhanced MAS NMR techniques at low temperatures (*ca.* 100 K),[2–5] provide significantly enhanced NMR signal sensitivity that allows the detection and analysis of heteroatom and ^{29}Si environments in zeolites at natural ^{29}Si isotopic abundance (4.7%).[6–11] The DNP NMR experiments use continuous microwave irradiation at *ca.* 100 K to transfer high electron spin polarization from stable nitroxide biradicals, such as TEKPol,[12] via hyperfine interactions to ^{1}H nuclei of frozen DNP solvent molecules, such as 1,1,2,2-tetrachloroethane (TCE), which was used here. The hydrophobic solvent TCE was chosen so as not to perturb the structure or hydration environments of ^{29}Si species in the zeolite framework. The DNP-enhanced ^{1}H spin polarization was distributed by ^{1}H-^{1}H spin diffusion through the frozen solvent to other nearby (<1 nm) solvent molecules, to the surface of the zeolite particles, and into the nanopores. Subsequently, DNP-enhanced ^{1}H polarization was transferred via ^{29}Si{^{1}H} cross-polarization (CP) to ^{29}Si nuclei in the zeolite framework, resulting in more than an order-of-magnitude enhancement in ^{29}Si signal intensity. Such increased signal sensitivity enables the measurement of two-dimensional (2D) ^{29}Si{^{29}Si} correlation spectra, which as discussed below have been challenging to acquire for nuclear-dipole-mediated (through-space) measurements and entirely unfeasible for *J*-mediated (through-covalent-bond) measurements, without expensive isotopic enrichment in ^{29}Si.

Q^3 and Q^4 ^{29}Si environments in natural abundance calcined Si-SSZ-70

Molecular interactions among organic solvent molecules, residual SDA molecules, adsorbed water, and framework Q^3 and Q^4 silicate species in calcined zeolite Si-SSZ-70 are established by using 2D DNP-enhanced NMR methods to measure and correlate their respective isotropic chemical shifts. For example, 2D ^{29}Si{^{1}H} or ^{13}C{^{1}H} DNP-enhanced HETeronuclear CORrelation (HETCOR) methods selectively detect ^{29}Si or ^{13}C or species that are dipole-dipole-coupled to ^{1}H nuclei that are in close molecular proximities (<1 nm). The resulting 2D NMR spectra are plotted as 2D frequency contour maps with normalized ^{1}H and ^{29}Si or ^{13}C chemical shift axes (Hz/MHz or ppm), such as shown in Figures 8, 9, **Error! Reference source not found.**, and S5 where the 2D intensity correlations establish the site-specific interactions and relative proximities of dipole-dipole coupled ^{29}Si or ^{13}C and ^{1}H nuclei. For example, the 2D DNP-enhanced ^{29}Si{^{1}H} HETCOR spectra in Figures 8 and **Error! Reference source not found.** demonstrate that Q^3 -SiOH moieties in the calcined zeolite Si-SSZ-70 framework exhibit hydrogen bonding interactions that are consistent with structural Models 1 and 2. The 2D spectra yield improved spectral resolution compared to the 1D ^{29}Si{^{1}H} CPMAS spectra shown above the 2D contour maps, which enables the detection of a number of distinct correlated ^{1}H-^{29}Si signals. Spectral resolution in the ^{1}H dimension is improved by the application of ^{1}H-^{1}H homonuclear decoupling during the evolution time to mitigate the influence of strong ^{1}H-^{1}H dipolar interactions among ^{1}H nuclei on the Si-SSZ-70 framework and TCE solvent molecules. To demonstrate the improved resolution of the 2D spectra, Figure S4 shows 1D slices extracted at ^{1}H shifts of 4.0, 7.2, and 8.8 ppm from the 2D spectrum acquired at very short ^{29}Si{^{1}H} contact times (0.2 ms) in Figures 8 and **Error! Reference source not found.**a. Different ^{29}Si signals at -96, -99, -105, -110, -113, and -114 ppm are each resolved in at least one of the horizontal slices, indicating that the different ^{29}Si species are in close molecular proximity within 0.5 nm for short contact times, e.g., 0.2 ms) to ^{1}H moieties at the corresponding ^{1}H chemical shifts. For example, in the 2D spectrum acquired at very short ^{29}Si{^{1}H} contact times (0.2 ms) in Figures 8 and S3a, ^{1}H signals are detected in the chemical shift range 2.0 to 4.4 ppm from relatively isolated -SiOH groups that are correlated with ^{29}Si signals in the range -95 to -103 ppm from silanol Q^3 ^{29}Si species, as expected, and also at -105 ppm from Q^4 ^{29}Si species that are in close proximities to silanol moieties such as Si2b in Model 1. The presence of isolated silanol groups that exhibit little hydrogen bonding is consistent with

models 1 and 3 of calcined Si-SSZ-70 shown in **Error! Reference source not found.**10. There are also ^{1}H signals at 6.5 and 7.2 ppm which arise from the DNP solvent (1,1,2,2-tetrachloroethane, TCE) which are correlated with all of the ^{29}Si signals, indicating that the TCE solvent molecules have entered into the zeolite nanopores, and are present both in the inter- and intralayer channel systems.

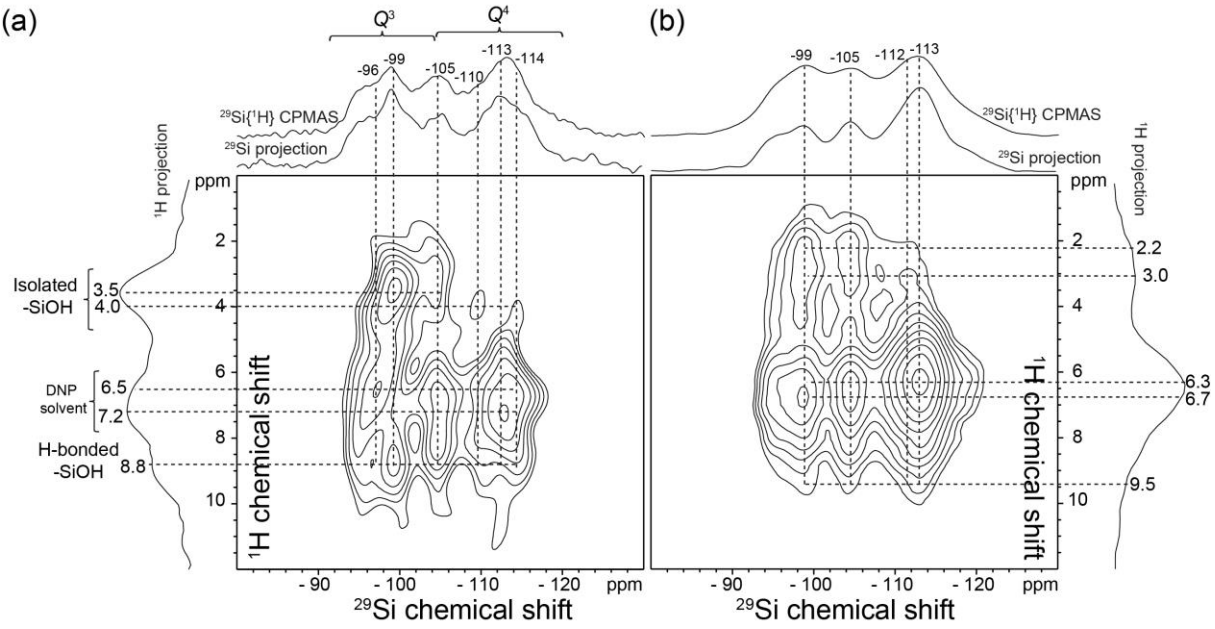

Figure S3. Solid-state DNP-enhanced 2D ^{29}Si{^{1}H} dipolar-mediated HETCOR spectra of calcined Si-SSZ-70 acquired in the presence of 16 mM TEKPol biradical in frozen tetrachloroethane, at 9.4 T, 95 K, 8 kHz MAS, with microwave irradiation at 263 GHz, and with different contact times of (a) 0.2 ms (same spectrum as Figure 8) and (b) 5 ms. 1D ^{29}Si{^{1}H} DNP-CPMAS spectra acquired under the same conditions are shown along the horizontal axes for comparison with the 1D projections of the 2D spectra. The signal-to-noise ratios of the 2D spectra in (a) and (b) are 11 and 67, respectively.

Importantly, high frequency ^{1}H signals in the chemical shift range 8 to 10 ppm arise from H-bonded -SiOH groups that are correlated with ^{29}Si signals from Q^3 silanol species at -93 to -103 ppm, and also with ^{29}Si signals from Q^4 species at -105 to -115 ppm. ^{1}H signals from H-bonded -SiOH groups over this range of ^{1}H frequencies are consistent with predictions based on empirical relations for ^{1}H isotropic chemical shifts as functions of -SiOH··OSi- distance in silicate glasses and minerals.[13,14] The shortest -OH··O distances (2.8 Å) associated with -SiOH··OHSi- hydrogen bonds in Models 2 and 3 (**Error! Reference source not found.**9) are consistent with the ^{1}H signals in the region 8-10 ppm. The presences of both isolated and strongly H-bonded -SiOH species are consistent with all three of the candidate structures proposed for calcined zeolite Si-SSZ-70.

All of the distinct ^{29}Si moieties present in the calcined zeolite Si-SSZ-70 are in close molecular proximities to each other, as established by the 2D ^{29}Si{^{1}H} DNP-HETCOR spectrum acquired at a longer contact time (Figure S3b, 5 ms). The spectral resolution is reduced at the longer contact time because the spectrum manifests longer range ^{29}Si-^{1}H interactions, such that each ^{29}Si signal is correlated with a broader distribution of ^{1}H signals than at shorter contact times. Nevertheless, different ^{1}H signals are detected at 2.2 to 3.0 ppm from isolated -SiOH groups, 6.3 to 6.7 ppm from frozen TCE solvent molecules, and 9.5 ppm from H-bonded -SiOH groups. Importantly, these ^{1}H signals are all correlated with broad ^{29}Si signals with partially-resolved peak maxima at -96, -99, -105, -111, and -113 ppm, establishing the close mutual proximities (<1 nm) of the

corresponding ^{29}Si and ^{1}H environments. These results suggest that the different types of -SiOH moieties are intermixed over nanoscale dimensions.

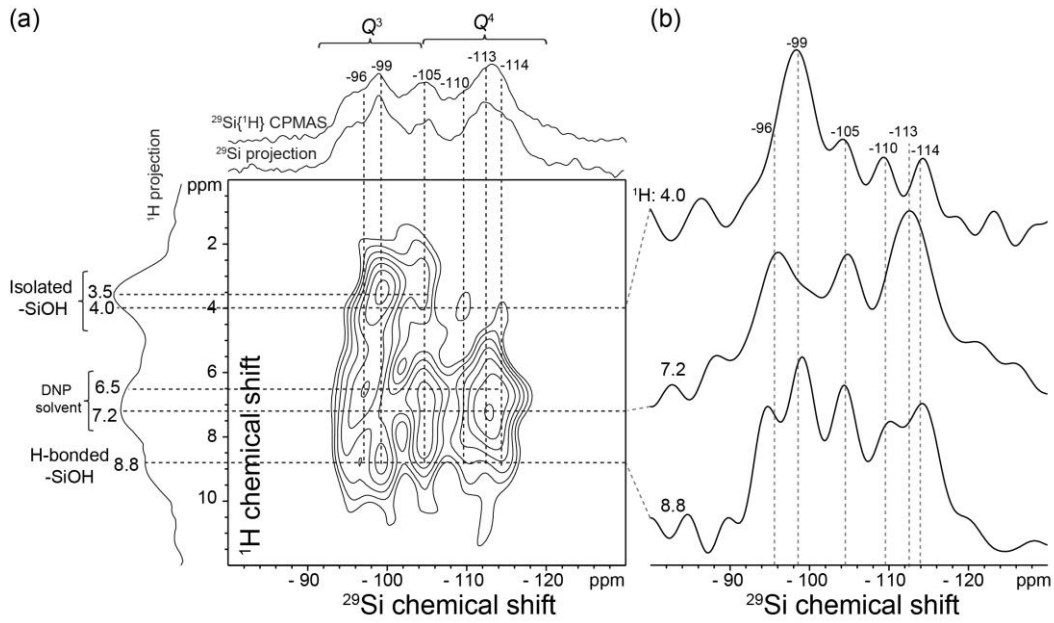

Figure 4. (a) Solid-state DNP-enhanced 2D ^{29}Si{^{1}H} dipolar-mediated HETCOR spectrum of calcined Si-SSZ-70 acquired in the presence of 16 mM TEKPol biradical in frozen tetrachloroethane, at 9.4 T, 95 K, 8 kHz MAS, with microwave irradiation at 263 GHz, and with a 0.2 ms contact time (same spectrum as Figures 8 and S3a). (b) Horizontal ^{29}Si slices extracted from the DNP-enhanced 2D ^{29}Si{^{1}H} dipolar-mediated HETCOR in Figure S3a at ^{1}H shifts of 4.0, 7.2, and 8.8 ppm. Dotted lines indicate the different ^{29}Si signals resolved in the 2D spectrum.

Residual OSDA in calcined SSZ-70

Interestingly, a small quantity of the organic *N,N'*-diisobutyl imidazolium cation structure directing agent (SDA)[15,16] used in the synthesis of Si-SSZ-70 is present in the calcined material, though was removed on subsequent drying of the sample at 200 °C. The small quantity of the organic SDA in calcined Si-SSZ-70 gives rise to ^{1}H signals that are assigned in the 2D ^{13}C{^{1}H} DNP-HETCOR spectrum in **Error! Reference source not found.**5. This spectrum yields improved ^{1}H spectral resolution compared to the 1D single-pulse ^{1}H spectrum that shows only a single broad signal at 6.1 ppm from ^{1}H moieties on the TCE solvent. The 2D ^{13}C{^{1}H} DNP-HETCOR spectrum enables the detection of additional ^{1}H signals at 7.2 and 8.8 ppm that are correlated with the ^{13}C signals at 131 and 122 ppm from imidazole carbon atoms 1 and 2, as indicated in the inset to the 2D spectrum, and are assigned to two different ^{1}H imidazole moieties. A ^{1}H signal is also detected at 2.8 ppm, which is correlated to ^{13}C signals at 59 ppm from carbon atoms 3 on the imidazole cation and is thus assigned to ^{1}H alkyl species. No correlated signal intensities from ^{13}C atoms 4 and 5 are detected in the 2D ^{13}C{^{1}H} DNP-HETCOR spectrum, likely because of the low absolute quantity of SDA molecules in the material and spectral broadening due to the freezing out of motions of alkyl sidechains on the SDA molecules at the low temperature conditions (95 K) used for DNP-NMR experiments. Furthermore, the percentage of residual SDA species can be estimated by comparing the relative integrated intensities of the ^{13}C signals resolved in the 1D ^{13}C{^{1}H} DNP-CPMAS spectrum shown above the 2D spectrum in **Error! Reference source not found.**5, which is dominated by a ^{13}C signal at 75 ppm from frozen DNP solvent TCE molecules. Weak ^{13}C signals from residual SDA species are also detected at 131, 123, 59, 31, and 16 ppm from ^{13}C atoms 1-5, respectively, on the SDA molecule as indicated in the inset to the 2D spectrum. While 1D ^{13}C{^{1}H} DNP-CPMAS NMR measurements are not strictly quantitative, by assuming that the ^{13}C signals from the frozen TCE and organic SDA molecules are all enhanced equally by DNP

(ε_C ~60) and have similar ^{13}C spin-spin and ^{1}H spin-lattice relaxation times, we estimate that the residual SDA comprises <0.4 wt% of the calcined Si-SSZ-70. The residual OSDA was removed by drying the calcined Si-SSZ-70 sample at 200 °C as described in the Experimental section, after which the spectra in Figures 8, 9, **Error! Reference source not found.**, S4, S7b, S8, and S9 were acquired.

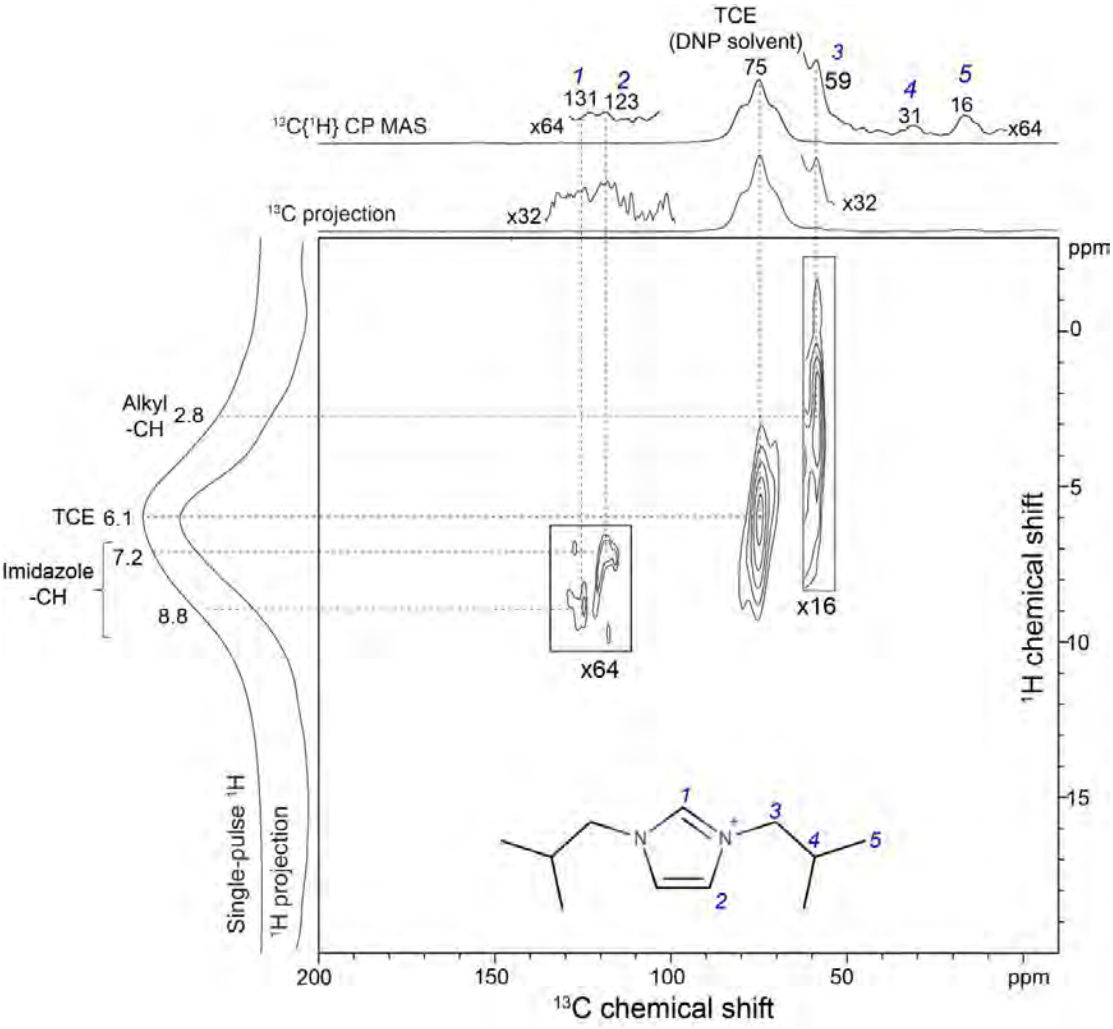

Figure S5. Solid-state 2D $^{13}C\{^{1}H\}$ DNP-HETCOR spectrum of calcined zeolite Si-SSZ-70 (without first drying at 200˚C), acquired in the presence of 16 mM TEKPol biradical in frozen tetrachloroethane, at 9.4 T, 95 K, 8 kHz MAS, with a contact time of 0.5 ms, and with microwave irradiation at 263 GHz. A single-pulse 1D ^{1}H MAS NMR spectrum and a 1D $^{13}C\{^{1}H\}$ DNP-CPMAS spectrum acquired under the same conditions are shown along the vertical and horizontal axes, respectively, for comparison with the 1D projections of the 2D spectrum. The inset shows a schematic diagram of the *N,N'*-diisobutyl imidazolium cation used as a structure-directing agent in the synthesis of SSZ-70.

Detecting and correlating covalent ^{29}Si-O-^{29}Si linkages

To establish unambiguously the covalent ^{29}Si-O-^{29}Si connectivities that distinguish the different interlayer structures of calcined Si-SSZ-70, the DNP-enhanced 2D $^{29}Si\{^{29}Si\}$ *J*-mediated correlation spectra (Figures 9a, S7b, S8, and S9) were acquired using the refocused INADEQUATE pulse sequence.[17,18] A schematic diagram of the DNP-enhanced *J*-mediated refocused INADEQUATE pulse sequence is shown in Figure S6. Through-bond *J* interactions between pairs of ^{29}Si nuclei are relatively weak (ca. 10-15 Hz), so that such measurements are

sensitive principally to ^{29}Si-O-^{29}Si nearest neighbor tetrahedral (T) site pairs. Due to the weak *J* interactions, such through-bond-mediated measurements have inherently low sensitivity. As a consequence, until recently the application of 2D ^{29}Si{^{29}Si} *J*-mediated NMR analyses of silicate solids has been limited to materials prepared with isotopic enrichment in ^{29}Si.[18] The sensitivity enhancements provided by DNP-NMR techniques enable the detection and analysis of covalently bonded ^{29}Si-O-^{29}Si moieties in solids at natural isotopic abundance of ^{29}Si (4.7%). Analyses of DNP-enhanced 2D ^{29}Si{^{29}Si} *J*-mediated correlation spectra have recently been used to study the connectivities of organosiloxane species grafted onto silica nanoparticles,[6] and elucidate the crystallization mechanisms of mesostructured zeolite framework structures.[11]

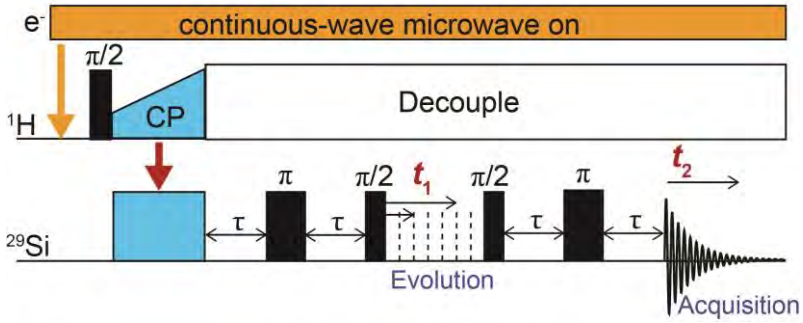

Figure S6. Schematic diagram of the DNP-enhanced 2D ^{29}Si{^{29}Si} CP-mediated refocused INADEQUATE experiment[11,17,18] used to acquire the 2D ^{29}Si{^{29}Si} spectra in Figures 9, S7, S8, and S9b. The rotor-synchronized delay time τ refocuses the chemical shift interaction and was experimentally optimized as discussed in the Experimental Section. The double-quantum coherences evolve during the incremented delay period t_1, and the signal is detected directly during the acquisition period t_2.

The efficiency of the refocused INADEQUATE experiment depends on the ratio of the spin-spin relaxation time T_2', as measured by a spin-echo experiment, to the apparent spin-spin relaxation time T_2*, which can be extracted from signal linewidths. The T_2'/T_2* ratio provides a measure of the extent of magnetization loss during the relatively long τ-π-τ periods that refocus the ^{29}Si-^{29}Si *J* interactions. A larger ratio (> 10) indicates that a greater fraction of the signal can be refocused, with higher resulting overall efficiency of the experiment.[17] The ^{29}Si T_2' relaxation time of calcined Si-SSZ-70 was measured by a spin-echo experiment under the same experimental conditions used to acquire the DNP-enhanced 2D ^{29}Si{^{29}Si} *J*-mediated correlation spectra, and found that T_2' = 13.5 ± 0.3 ms for all of the ^{29}Si signals. The T_2* times were estimated from deconvolution of the ^{29}Si spectra, and range from 0.8 to 1.2 ms for the different ^{29}Si signals. The ratio of ^{29}Si T_2'/T_2* is thus 11 or greater, indicating that approximately 90% of the spectral line width is due to inhomogeneous effects that are refocusable by the *J*-mediated experiment. The efficiency of the experiment is therefore high, consistent with previous refocused INADEQUATE analyses on partially-ordered solids. The large inhomogeneous components of the ^{29}Si linewidths likely arise from distributions of chemical shifts, due in part to the different types of interlayer structures, as well as to distributions of local ^{29}Si environments arising from interactions with the frozen TCE DNP solvent molecules.

Comparison of through-bond and through-space DNP-enhanced 2D ^{29}Si{^{29}Si} *J*- and dipolar-mediated correlation spectra

Compared to *J*-mediated spectra, dipolar-mediated spectra rely on through-space interactions between ^{29}Si-^{29}Si spin pairs, which, while stronger than *J* interactions, can arise from both covalently linked or non-covalently linked framework sites and thus are inherently ambiguous. Dipolar-mediated 2D ^{29}Si{^{29}Si} spectra yield greater signal sensitivity, and so for comparison with the DNP-enhanced 2D ^{29}Si{^{29}Si} *J*-mediated correlation spectrum of calcined Si-SSZ-70 (Figures 9a, S7b, S8b, and S9), a dipolar-mediated analogue was acquired (Figure S7). The dipolar-mediated spectrum was acquired using symmetry-based SR26$^4_{11}$ dipolar recoupling[19,20] and with a short recoupling time (3.4 ms) expected to yield good selectivity for ^{29}Si-^{29}Si spin pairs that are

< 5 Å separate.[21] Similar 2D intensity correlations are present in both the dipolar and *J*-mediated spectra (Fig. S7b), consistent with the expected signal contributions to the dipolar-mediated spectrum from pairs of nearest-neighbor ^{29}Si sites. However, the dipolar-mediated spectrum also exhibits a partially-resolved on-diagonal correlation at -105 ppm (blue box in Figure S7a) from through-space interactions between next-nearest-neighbour Q^4 Si2a-Si2a and Si2b-Si2b pairs. The signal arises because the Si2a-Si2a or Si2b-Si2b distance is relatively short (4.2 Å), and because Q^4 Si2a and Si2b together comprise a substantial fraction (ca. 13%) of the ^{29}Si species in the material, with relatively narrow ^{29}Si signals that are well-resolved in the 2D dipolar-mediated spectrum. Because of the potential for ambiguity with the dipolar-mediated analyses, we have emphasized the *J*-mediated analyses, which provide clear unambiguous evidence for the different types of ^{29}Si-O-^{29}Si covalent linkages that are crucial to understanding the interlayer structure of calcined Si-SSZ-70. In the past, dipolar-mediated spectra were principally used in spite of the ambiguities, because the weak *J* interactions and low (4.7%) isotopic abundance of ^{29}Si rendered 2D ^{29}Si{^{29}Si} *J*-mediated correlation spectra entirely unfeasible to acquire without isotopic enrichment in ^{29}Si. Acquisition of 2D ^{29}Si{^{29}Si} *J*-mediated correlation spectra has been enabled here on natural abundance materials by enhancements provided by DNP-NMR.

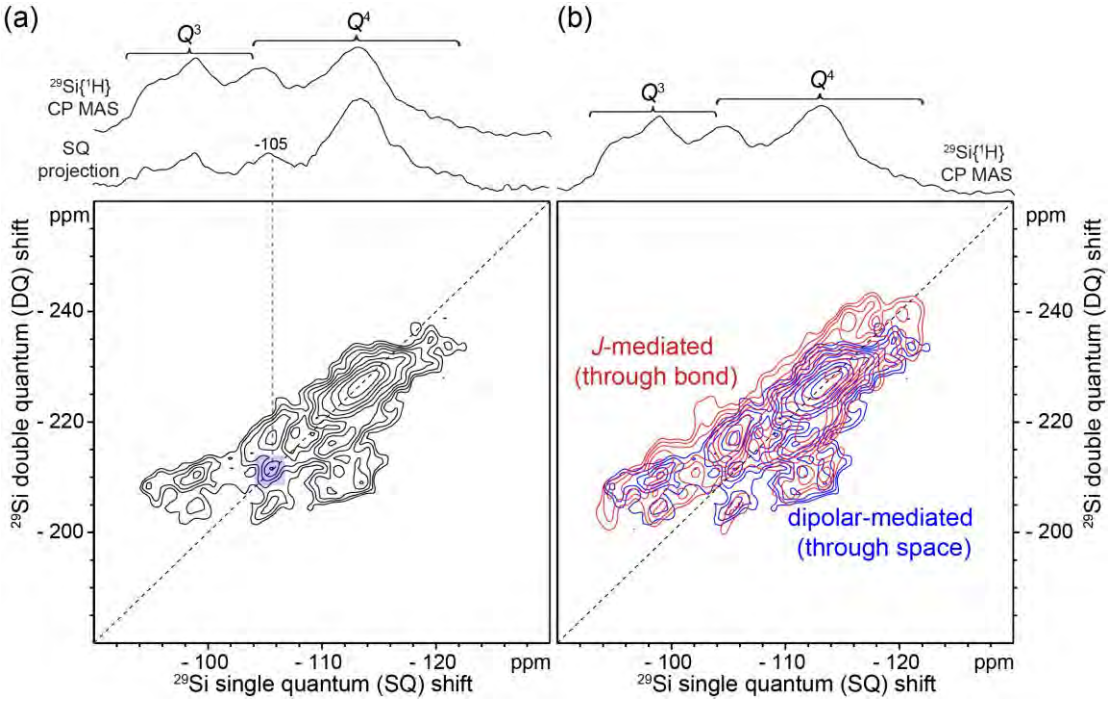

Figure S7. Solid-state DNP-enhanced 2D ^{29}Si{^{29}Si} dipolar-mediated correlation spectrum of calcined Si-SSZ-70 acquired at 9.4 T, 298 K, 4.6 kHz MAS, and using symmetry-based SR26$^4_{11}$ dipolar recoupling with 3.4 ms excitation and reconversion blocks to reintroduce the ^{29}Si-^{29}Si dipole-dipole couplings. A 1D ^{29}Si{^{1}H} DNP-CPMAS spectrum acquired at 8 kHz MAS but under otherwise the same conditions is shown along the vertical axis for comparison with the 1D projection of the 2D spectrum. The signal-to-noise ratio of the 2D spectrum is 17. (b) Comparison of the DNP-enhanced 2D ^{29}Si{^{29}Si} *J*- (red, same spectrum as Fig. 9a, S6b, and S7) and dipolar-mediated (blue, same spectrum as (a)) correlation spectra of calcined Si-SSZ-70.

Comparison to ITQ-1

To better identify and assign the ^{29}Si signals in the DNP-enhanced 2D ^{29}Si{^{29}Si} *J*-mediated correlation spectrum of calcined Si-SSZ-70 (Figure 9a), a similar DNP-NMR analysis was conducted on an ITQ-1 sample (**Error! Reference source not found.**). An impurity phase was identified in this ITQ-1 sample by synchrotron XRPD, which contributes to the overall signal sensitivity of the 2D *J*-mediated spectrum and gives rise to a number of correlated signals in the DNP-enhanced 2D *J*-mediated ^{29}Si{^{29}Si} spectrum in Figure S8a that have not been assigned and

overlap with some of the ^{29}Si signals from sites in the ITQ-1 framework. Nonetheless, several ^{29}Si signals can be resolved and assigned to key structural features that are shared by both ITQ-1 and calcined zeolite Si-SSZ-70. Specifically, the signal at -105 ppm is assigned to Si2 on the basis of past ^{29}Si NMR analysis of ITQ-1[22] and semi-empirical ^{29}Si shift calculations as described in the main text. This signal is correlated to partially-resolved ^{29}Si signals at -112 and -113 ppm (blue lines) which are assigned to Si3 and overlapping signals from Si4 and Si1, respectively. Assignment of the remaining signals resolved in the spectrum in **Error! Reference source not found.**a to the ^{29}Si T-sites in ITQ-1 is impeded by the presence of the impurity phase and the low signal-to-noise ratio of the *J*-mediated spectrum. However, comparison to the analogous spectrum of calcined Si-SSZ-70 (Figure S8b) shows that the signals from Si2 (or Si2b), Si4 (or Si4b), Si3, and Si1 (or Si1a) are in similar shift positions for both materials. Key differences include broader ^{29}Si signals in the spectrum of calcined Si-SSZ-70, likely due to the presence of distinct but very similar T-sites (e.g., Si5a/Si5b, Si8a/Si8b, etc.) which have overlapping ^{29}Si signals. Signals in the 2D spectrum of ITQ-1 that do not overlap with the spectrum of calcined Si-SSZ-70 likely arise from the impurity phase. Notably the signals from Si2, Si3, and Si4 Q^4 T sites are similar for both materials, enabling the more detailed analysis and assignment of the ^{29}Si spectrum of calcined Si-SSZ-70 discussed below and in the main text.

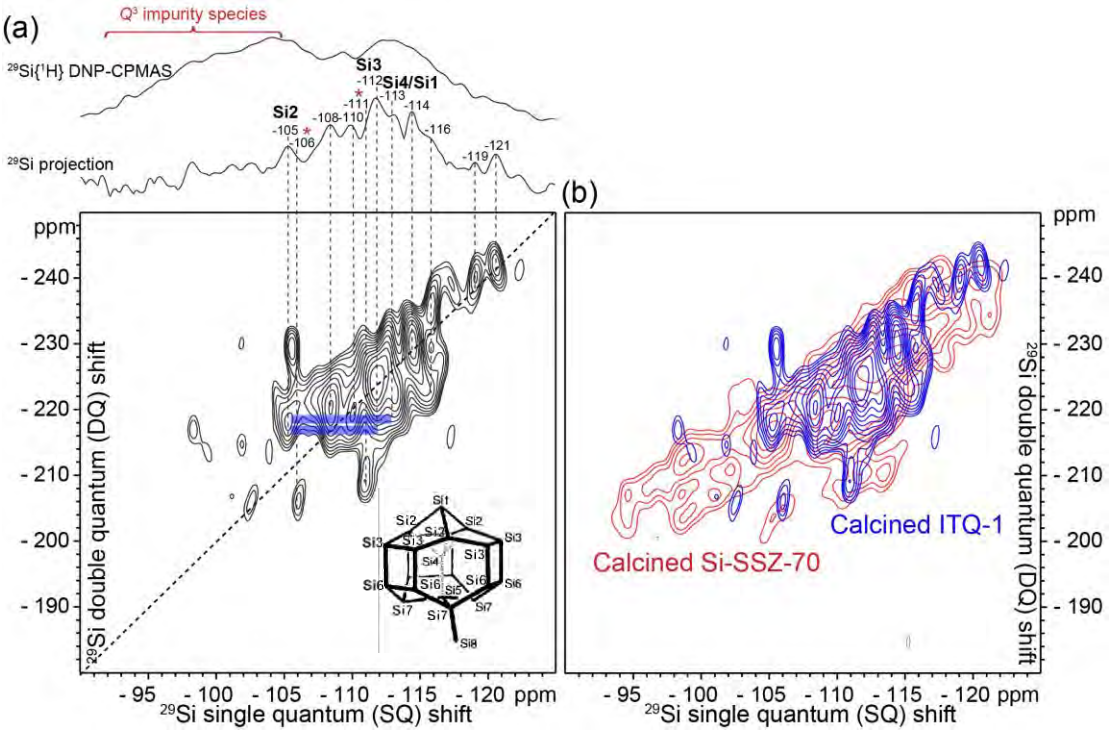

Figure S8. (a) Solid-state DNP-enhanced 2D ^{29}Si{^{29}Si} *J*-mediated correlation spectrum of ITQ-1. A 1D ^{29}Si{^{1}H} DNP-CPMAS spectrum acquired under the same conditions is shown along the horizontal axis for comparison with the 1D projection of the 2D spectrum. Signals assigned to an impurity phase are indicated by asterisks. The inset shows the structure of ITQ-1 with all T-sites labeled, adapted from [22]. The signal-to-noise ratio of the 2D spectrum is 4. (b) Comparison of the DNP-enhanced 2D ^{29}Si{^{29}Si} *J*-mediated correlation spectra of ITQ-1 (blue, same spectrum as (a)) and calcined Si-SSZ-70 (red, same spectrum as Figure 9a).

Covalent framework ^{29}Si-O-^{29}Si connectivities in calcined Si-SSZ-70

As discussed in the main text, multiple covalent connectivities among distinct Q^3 and Q^4 ^{29}Si species that are consistent with the proposed structural models of calcined zeolite Si-SSZ-70 are resolved in the 2D ^{29}Si{^{29}Si} DNP-enhanced *J*-mediated correlation spectrum shown in Figures 9a, S7b, S8b, and S9. The spectrum is dominated by broad ^{29}Si signal intensity that straddles the diagonal centered at -114 ppm, which arises from overlapping signals associated with covalently

bonded ^{29}Si-O-^{29}Si moieties among the different framework Q^4 sites in calcined zeolite Si-SSZ-70. ^{29}Si signals in the spectral region -105 to -122 ppm are assigned to Q^4 T-sites in the **MWW**-type layers of calcined Si-SSZ-70, and their shifts are consistent with past results on similar zeolites[22,23] and shift values calculated using the proposed models of calcined zeolite Si-SSZ-70 and well-established semi-empirical relationships.[19,24] The signals are broadened due to interactions with frozen TCE solvent molecules in the zeolite nanopores; nevertheless, the resolution provided by the 2D spectrum is sufficient to partially resolve pairs of correlated signal intensity at ^{29}Si indicated by the solid lines in Figure S9, which arise from the covalent interconnectivities of different framework T-sites. These ^{29}Si signals are tabulated and assigned on the basis of their shift values and covalent connectivities in Table S1. We note that the signal at -95.0 ppm from Model 2 Si2b silanol moieties is missing its correlated signal pair, which is expected to be at *ca*. -112 ppm and is probably absent because of the low absolute quantities of the corresponding ^{29}Si species and differences in T_2 spin-spin relaxation times.

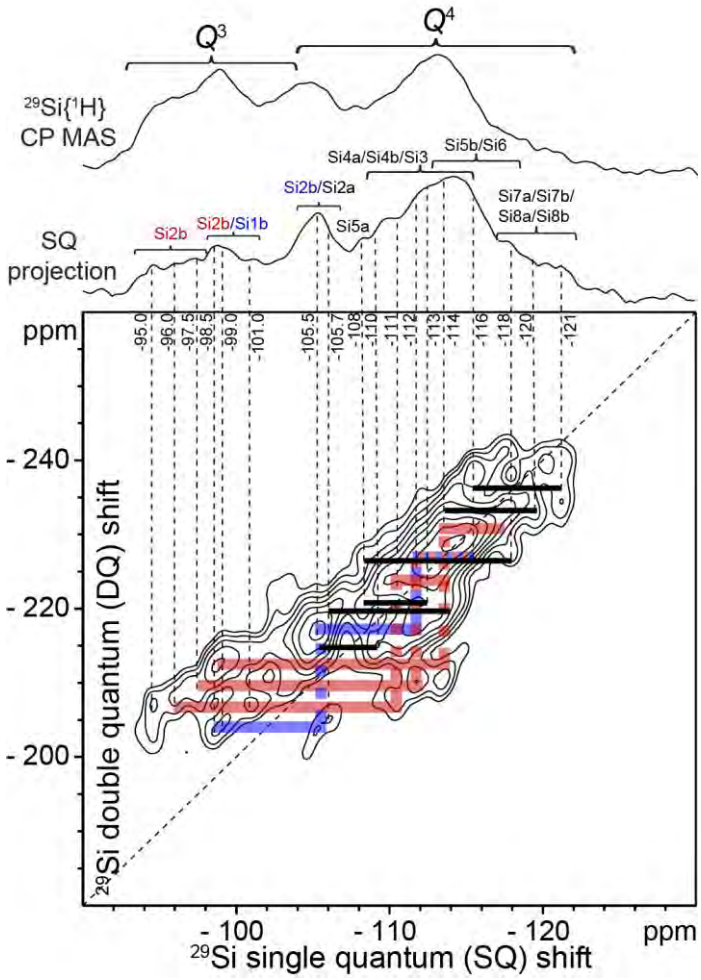

Figure S9. Solid-state DNP-enhanced 2D ^{29}Si{^{29}Si} *J*-mediated correlation spectrum of calcined Si-SSZ-70 (same spectrum as Figures 10a and S6b). A 1D ^{29}Si{^{1}H} DNP-CPMAS spectrum acquired under the same conditions is shown along the vertical axis for comparison with the 1D projection of the 2D spectrum. 2D intensity correlations associated with covalent connectivities of Q^3 and Q^4 ^{29}Si species that are consistent with model 1 and model 2 are indicated by blue and red lines, respectively, while those associated with Q^4 ^{29}Si-O-^{29}Si connectivities shared by both models are indicated by black lines. The signal-to-noise ratio of the 2D spectrum is 15.

Table S1. ^{29}Si NMR signal assignments to ^{29}Si sites in calcined Si-SSZ-70, based on the DNP-enhanced 2D ^{29}Si{^{29}Si} *J*-mediated NMR results.

^{29}Si chemical shift (ppm)	Type	Assignment
-94.5	Q^3	Si2b (Model 2)
-96.0		
-97.5	Q^3	Si2b (Model 2) Si1b (Model 1)
-98.5		
-99.0		
-101.0		
-105.5	Q^4	Si2b (Model 1) Si2a
-105.7		
-108	Q^4	Si5a
-110	Q^4	Si4b, Si4a
-111	Q^4	Si4b, Si4a, Si3
-112		
-113		
-114	Q^4	Si4b, Si4a, Si3, Si5b
-116	Q^4	Si5b, Si6
-118	Q^4	Si7a, Si7b, Si8a, Si8b
-120		
-121		

Model 3

Initially, we hypothesized a third model, referred to as Model 3, where another 3-ring takes the place of the terminal SiOH (**Error! Reference source not found.**10). In comparison to Models 1 and 2, there is less compelling evidence for the candidate structure depicted in Model 3. Based on ^{29}Si shift values calculated from semi-empirical relations,[19,24] Q^4 T-sites S2b and Si3 in Model 3 would be expected to exhibit overlapping ^{29}Si signals in the range of -107 to -110 ppm, while Q^4 T-sites Si4b and Si5b would exhibit ^{29}Si signals in the ranges of -116 to -119 ppm and -118 ppm to -121 ppm, respectively. Thus, the four-T-site covalent interconnectivity paths between the Q^3 silanol moieties and the Q^4 T-sites in the **MWW** cages (Si19-O-Si12-O-Si14-O-Si15 and Si19-O-Si12-O-Si3-O-Si6) expected for model 3 would yield distinct correlated ^{29}Si signal pairs at approximate shift values of (-95, -109) for Si1c-O-Si2b, (-109, -116) from Si3-O-Si6, (-109, -118) from Si2b-O-Si4b, and (-118, -120) from Si4b-O-Si5b. Broad signal intensity in these regions is detected, which could possibly be assigned to Q^3 and Q^4 T-sites in Model 3, though which are not resolved. If present, such correlated pairs of signals could not be distinguished from those associated with interconnected Q^4 ^{29}Si T-sites in the intralayer channel which are expected to be the same for all three candidate structures. Thus, while Model 3 cannot be definitively ruled out, the absence of clear evidence for silicate T-site structural connectivities that are assignable to Model 3 suggests that this candidate structure is less likely to be present, within the resolution limits of the measurements. In contrast, the 2D DNP-enhanced *J*-mediated ^{29}Si{^{29}Si} NMR correlation spectrum of calcined Si-SSZ-70 provides clear evidence for the presence of distinct Q^3 silanol species with covalent connectivities that are consistent with candidate structural Models 1 and 2, as discussed above. Additionally, the total quantity of Q^3 silicate species present in the material is ca. 6% (Figure 9b),which is consistent with roughly 50% of calcined Si-SSZ-70 being structurally consistent with Model 1 and 50% with Model 2.

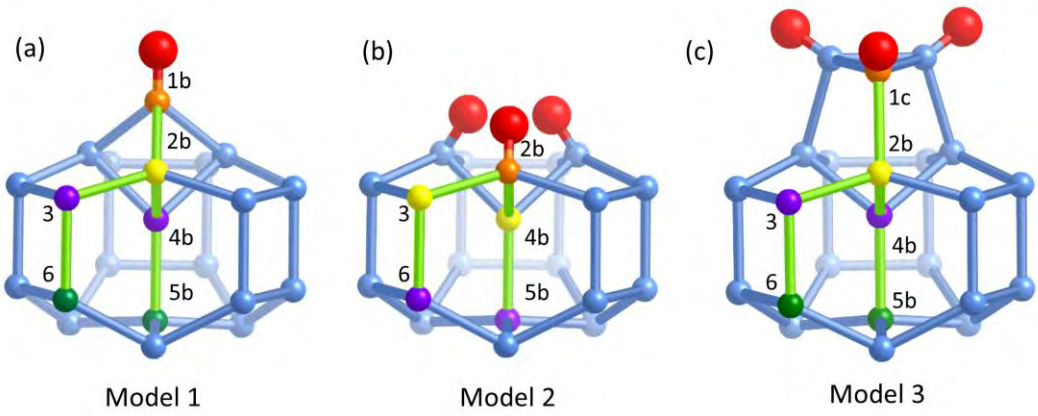

Figure S10. Proposed candidate structures of calcined zeolite Si-SSZ-70 showing the differences in interlayer structure with the distinguishing connectivities indicated with green lines for (a) Model 1, (b) Model 2, and (c) Model 3.

References

(1) Stadelmann, P. A. *JEMS - EMS Java version*; 2004.

(2) Maly, T.; Debelouchina, G. T.; Bajaj, V. S.; Hu, K.-N.; Joo, C.-G.; Mak–Jurkauskas, M. L.; Sirigiri, J. R.; van der Wel, P. C. A.; Herzfeld, J.; Temkin, R. J.; Griffin, R. G. *J. Chem. Phys.* **2008**, *128* (5), 052211.

(3) Lesage, A.; Lelli, M.; Gajan, D.; Caporini, M. A.; Vitzthum, V.; Miéville, P.; Alauzun, J.; Roussey, A.; Thieuleux, C.; Mehdi, A.; Bodenhausen, G.; Coperet, C.; Emsley, L. *J. Am. Chem. Soc.* **2010**, *132* (44), 15459–15461.

(4) Ni, Q. Z.; Daviso, E.; Can, T. V.; Markhasin, E.; Jawla, S. K.; Swager, T. M.; Temkin, R. J.; Herzfeld, J.; Griffin, R. G. *Acc. Chem. Res.* **2013**, *46* (9), 1933–1941.

(5) Rossini, A. J.; Zagdoun, A.; Lelli, M.; Lesage, A.; Copéret, C.; Emsley, L. *Acc. Chem. Res.* **2013**, *46* (9), 1942–1951.

(6) Lee, D.; Monin, G.; Duong, N. T.; Lopez, I. Z.; Bardet, M.; Mareau, V.; Gonon, L.; De Paëpe, G. *J. Am. Chem. Soc.* **2014**, *136* (39), 13781–13788.

(7) Wolf, P.; Valla, M.; Rossini, A. J.; Comas-Vives, A.; Núñez-Zarur, F.; Malaman, B.; Lesage, A.; Emsley, L.; Copéret, C.; Hermans, I. *Angew. Chem. Int. Ed.* **2014**, *53* (38), 10179–10183.

(8) Gunther, W. R.; Michaelis, V. K.; Caporini, M. A.; Griffin, R. G.; Román-Leshkov, Y. *J. Am. Chem. Soc.* **2014**, *136* (17), 6219–6222.

(9) Sangodkar, R. P.; Smith, B. J.; Gajan, D.; Rossini, A. J.; Roberts, L. R.; Funkhouser, G. P.; Lesage, A.; Emsley, L.; Chmelka, B. F. *J. Am. Chem. Soc.* **2015**, *137* (25), 8096–8112.

(10) Wolf, P.; Valla, M.; Núñez-Zarur, F.; Comas-Vives, A.; Rossini, A. J.; Firth, C.; Kallas, H.; Lesage, A.; Emsley, L.; Copéret, C.; Hermans, I. *ACS Catal.* **2016**, *6* (7), 4047–4063.

(11) Berkson, Z. J.; Messinger, R. J.; Na, K.; Seo, Y.; Ryoo, R.; Chmelka, B. F. *Angew. Chem. Int. Ed.* **2017**, *56* (19), 5164–5169.

(12) Zagdoun, A.; Casano, G.; Ouari, O.; Schwarzwälder, M.; Rossini, A. J.; Aussenac, F.; Yulikov, M.; Jeschke, G.; Copéret, C.; Lesage, A.; Tordo, P.; Emsley, L. *J. Am. Chem. Soc.* **2013**, *135* (34), 12790–12797.

(13) Yesinowski, J. P.; Eckert, H.; Rossman, G. R. *J. Am. Chem. Soc.* **1988**, *110* (5), 1367–1375.

(14) Xue, X.; Kanzaki, M. *J. Am. Ceram. Soc.* **2009**, *92* (12), 2803–2830.

(15) Archer, R. H.; Carpenter, J. R.; Hwang, S.-J.; Burton, A. W.; Chen, C.-Y.; Zones, S. I.; Davis, M. E. *Chem. Mater.* **2010**, *22* (8), 2563–2572.

(16) Archer, R. H.; Zones, S. I.; Davis, M. E. *Micropor. Mesopor. Mat.* **2010**, *130* (1–3), 255–265.

(17) Lesage, A.; Bardet, M.; Emsley, L. *J. Am. Chem. Soc.* **1999**, *121* (47), 10987–10993.

(18) Cadars, S.; Mifsud, N.; Lesage, A.; Epping, J. D.; Hedin, N.; Chmelka, B. F.; Emsley, L. *J. Phys. Chem. C* **2008**, *112* (25), 9145–9154.

(19) Brouwer, D. H.; Darton, R. J.; Morris, R. E.; Levitt, M. H. *J. Am. Chem. Soc.* **2005**, *127* (29), 10365–10370.

(20) Brouwer, D. H.; Kristiansen, P. E.; Fyfe, C. A.; Levitt, M. H. *J. Am. Chem. Soc.* **2005**, *127* (2), 542–543.

(21) Perras, F. A.; Padmos, J. D.; Johnson, R. L.; Wang, L.-L.; Schwartz, T. J.; Kobayashi, T.; Horton, J. H.; Dumesic, J. A.; Shanks, B. H.; Johnson, D. D.; Pruski, M. *J. Am. Chem. Soc.* **2017**, *139* (7), 2702–2709.

(22) Camblor, M. A.; Corma, A.; Díaz-Cabañas, M.-J.; Baerlocher, C. *J. Phys. Chem. B* **1998**, *102* (1), 44–51.

(23) Camblor, M. A.; Corell, C.; Corma, A.; Díaz-Cabañas, M.-J.; Nicolopoulos, S.; González-Calbet, J. M.; Vallet-Regí, M. *Chem. Mater.* **1996**, *8* (10), 2415–2417.

(24) Lewis, J. E.; Freyhardt, C. C.; Davis, M. E. *J. Phys. Chem.* **1996**, *100* (12), 5039–5049.